

# Physical processes influencing acoustic radiation from jet engine inlets

Christopher K. W. Tam<sup>1,†</sup>, Sarah A. Parrish<sup>1</sup>, Edmane Envia<sup>2</sup>  
and Eugene W. Chien<sup>3</sup>

<sup>1</sup>Department of Mathematics, Florida State University, Tallahassee, FL 32306-4510, USA

<sup>2</sup>NASA Glenn Research Center, Cleveland, OH 44135, USA

<sup>3</sup>Goodrich Aerostructures Group, Chula Vista, CA 91910, USA

(Received 7 July 2012; revised 21 February 2013; accepted 4 April 2013)

Numerical simulations of acoustic radiation from a jet engine inlet are performed using advanced computational aeroacoustics algorithms and high-quality numerical boundary treatments. As a model of modern commercial jet engine inlets, the inlet geometry of the NASA Source Diagnostic Test is used. Fan noise consists of tones and broadband sound. This investigation considers the radiation of tones associated with upstream-propagating duct modes. The primary objective is to identify the dominant physical processes that determine the directivity of the radiated sound. Two such processes have been identified. They are acoustic diffraction and refraction. Diffraction is the natural tendency for an acoustic duct mode to follow a curved solid surface as it propagates. Refraction is the turning of the direction of propagation of a duct mode by mean flow gradients. Parametric studies on the changes in the directivity of radiated sound due to variations in forward flight Mach number, duct mode frequency, azimuthal mode number and radial mode number are carried out. It is found there is a significant difference in directivity for the radiation of the same duct mode from an engine inlet when operating in static condition versus one in forward flight. It will be shown that the large change in directivity is the result of the combined effects of diffraction and refraction.

**Key words:** acoustics, aeroacoustics

---

## 1. Introduction

Acoustic radiation from jet engine inlets has been studied experimentally by Heidmann, Saule & McArdle (1980), Preisser *et al.* (1985), Heidelberg (2002), Premo & Joppa (2002), Woodward *et al.* (2002), Herkes, Olser & Uellenberg (2006), Yu *et al.* (2006), Callender *et al.* (2007) and Lan *et al.* (2007), analytically by Lansing (1970), Homicz & Lordi (1975), Kempton & Smith (1982) and Dougherty (1996), and computationally by Baumeister & Horowitz (1984), Eversman *et al.* (1985), Parrett & Eversman (1986), Roy & Eversman (1995), Ozyoruk & Long (1996), Ahuja, Ozyoruk & Long (2000), Astley *et al.* (2002), Ozyoruk (2002), Zhang *et al.* (2002), Ozyoruk *et al.* (2004), Premo, Bread & Lan (2007) and Achunche *et al.* (2009) in the past.

† Email address for correspondence: [tam@math.fsu.edu](mailto:tam@math.fsu.edu)

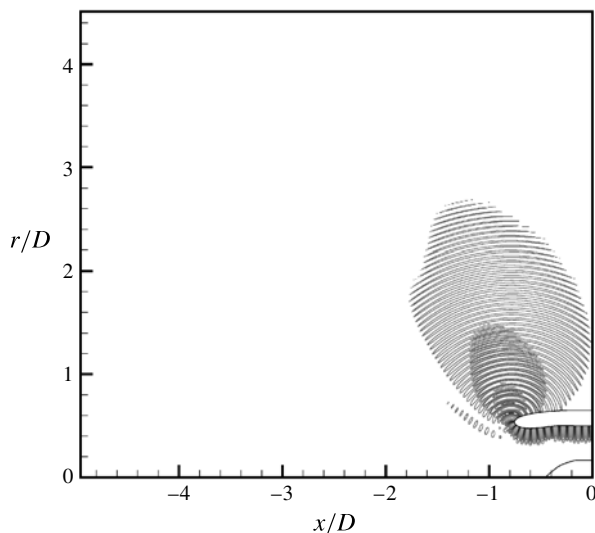


FIGURE 1. Computed pressure contour pattern of an  $m = 22$ ,  $n = 1$  duct mode at 6400 Hz radiating out of the SDT fan inlet;  $M_{fan} = 0.4$ ,  $M_{flight} = 0$  (static condition).

These studies provide a variety of useful and interesting information. They also provide prediction capabilities and methods. It is known that sound radiated out of an engine inlet consists of both broadband noise and tones. Broadband fan noise is random and chaotic and is best studied statistically. Tones, on the other hand, which are generated by the fan rotating at high speeds and by the cutting of the rotor wake by the stator blades, are highly organized and propagate coherently. In the inlet duct, tones propagate as duct modes. Because duct modes are coherent propagating entities, they are readily open to analysis and numerical simulation. Their propagation characteristics are also easy to understand. Duct mode propagation from the fan face to the far field is the subject of the present investigation.

It is our belief that the mechanisms that influence the radiation of duct modes operate independently of the engine inlet geometry; the geometry of the engine inlet does, however, alter the relative importance of the various mechanisms. For this reason, this study primarily uses the inlet geometry of the NASA Source Diagnostic Test (SDT) fan, which has internal fan duct diameter of 22 inches at the fan face. The fan has 22 blades. The inlet geometry of the SDT fan is typical of most modern high-bypass-ratio jet engines.

There is significant complexity in the duct mode radiation processes. To illustrate this point, consider the radiation patterns associated with the NASA SDT fan inlet in figures 1 and 2. The flow Mach number at the fan face is the same for both cases:  $M_{fan} = 0.4$ . The duct mode radiating out of the inlet is also the same in each case, and is defined with azimuthal mode number  $m = 22$ , radial mode number  $n = 1$  and frequency  $f = 6400$  Hz. Figure 1 shows the pressure contour pattern for the engine at static condition, i.e. no forward flight. Figure 2 shows the pressure contour pattern when the engine is moving with forward flight Mach number 0.2. Figures 1 and 2 are representative of the simulations to be described in the rest of this paper. It is obvious that the dominant directions of radiation in the two cases are substantially different.

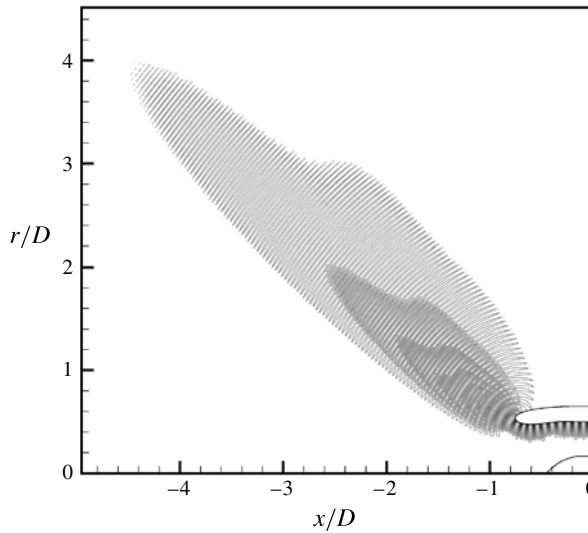


FIGURE 2. Computed pressure contour pattern of an  $m = 22$ ,  $n = 1$  duct mode at 6400 Hz radiating out of the SDT fan inlet;  $M_{fan} = 0.4$ ,  $M_{flight} = 0.2$ .

But why are they so different for such a low flight Mach number? Currently, a valid explanation does not appear to be available in the open literature.

Thus, in spite of past studies, there seems to be a need for further effort in the investigation of the flow physics that controls and influences the acoustic radiation processes. This is the purpose of the present investigation. To accomplish this goal, numerical simulation using advanced computational aeroacoustics (CAA) methods is used. We would like to point out that, for the stated purpose, numerical simulation has some significant advantages over an experimental investigation. This does not mean that experiments are unimportant. Actually, they are absolutely necessary for validation and other purposes. A few of these advantages are listed below.

(i) In a numerical simulation, there is full access to space and time data inside and outside an engine inlet. They include both the mean flow and acoustic disturbances. These types of data are needed in order to understand the physical processes involved in the radiation of a duct mode. In principle, these quantities can also be measured experimentally. But to do so would require an extraordinary effort; therefore, it has never been done.

(ii) Computationally, the amount of effort required to simulate engine inlet radiation with and without forward flight is about the same. Experimentally, studying the forward flight effect in a laboratory would require the use of a wind tunnel, which introduces background wind tunnel noise and possible extraneous tones from the facility. Complications also arise from wall reflection, if a closed wind tunnel is used, and from shear layer correction, if an open wind tunnel is used.

(iii) Numerical simulation allows an easy study of the radiation of an individual duct mode. A parametric study of the variation of mode frequency and azimuthal and radial mode numbers can easily be carried out. Experimentally, generating a single duct mode is no trivial matter. Usually, the measured pressure signal contains a multitude of modes. Unscrambling the measured pressure data in order to recover individual mode information is not an easy task.

In this paper, it is our intent to show that duct mode radiation from a jet engine inlet is greatly influenced by the effects of diffraction and refraction. Here, diffraction refers to the inherent characteristic of a duct mode to follow and remain attached to the wall of the engine casing as it propagates and eventually radiates away. Refraction is the turning of the direction of propagation of a duct mode by mean flow gradients. The degree of influence of these two effects is, however, highly dependent on fan face Mach number,  $M_{fan}$ , forward flight Mach number,  $M_{flight}$ , azimuthal and radial mode numbers,  $(m, n)$ , and frequency,  $f$ . The sum of all the individual effects ultimately determines the dominant direction of radiation for a duct mode. The present investigation focuses on finding the dependence of the diffraction and refraction effects on each of the above parameters. Reporting and explaining these results forms the main body of this paper. In addition, we will document the CAA methods and algorithms used, as they may be of interest to other investigators. To assure that our simulations are accurate, we have performed validation tests by comparing the computed directivity with experimental measurements.

The rest of the paper is as follows. In §2 we discuss the computational grid, computational model and algorithm, as well as various types of boundary conditions used in the present numerical simulations. The results of a series of computer code validation tests are reported in §3. Directivity data from a JT15D engine experiment (Heidmann *et al.* 1980; Heidelberg, Rice & Homyak 1981; Preisser *et al.* 1985) are used for comparison. In §4 we present computed mean flow data, both with and without forward flight, for the NASA STD engine inlet. Acoustic results are reported in §5. They include a detailed study of the effects of diffraction and refraction. An explanation for the large impact of forward flight on the direction of duct mode radiation is presented. A parametric study showing the effects of forward flight Mach number, duct mode frequency, and azimuthal and radial mode numbers on the radiation pressure contour pattern and directivity has been carried out. The results of this parametric study are reported in §6. The impact of diffraction and refraction effects on these results is explained. Finally, §7 gives a summary and conclusion of this work.

## 2. Computational model, grid design and computational algorithm

In this section, information on the computational domain, computational model, grid design and computational algorithm used in the present numerical simulation of jet engine inlet radiation is provided.

### 2.1. Grid design

Figure 3 shows the computational domain in physical space. The engine inlet is at the lower right corner. The internal diameter,  $D$ , of the casing at the fan face is used as the length scale. For the NASA STD fan,  $D$  is approximately 22 inches. There are 22 fan blades. The computational domain extends five diameters ( $5D$ ) in front of the fan face and four diameters ( $4D$ ) in the sideline direction. This is the size of the domain used for near-field pressure contour pattern computation. For validation directivity computations, the domain is extended further to the left by another  $5D$  and to the right, outside the inlet, by  $3D$ . To generate a body-fitted grid, a conformal mapping method is used (see Tam & Ju 2012 or Tam 2012). One advantage of using a conformal mapping is that it can generate a body-fitted grid for two or more isolated bodies. In the present problem, they are the casing and the hub. There does not seem to be another simple, body-fitted method available for generating this type of grid.

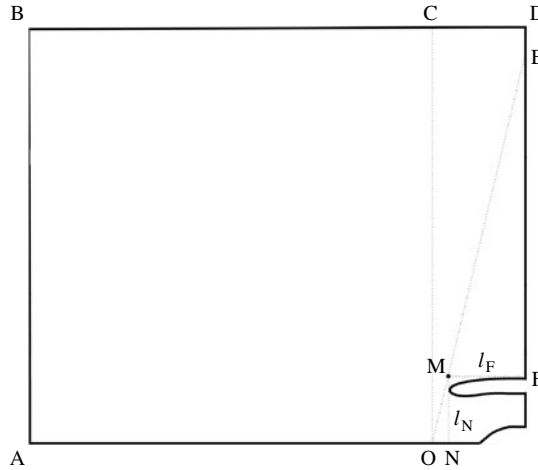


FIGURE 3. Computational domain for near-field pressure contour pattern computations.

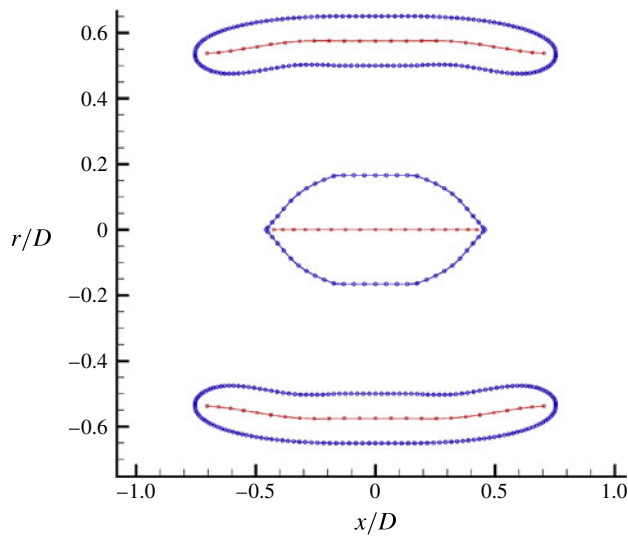


FIGURE 4. (Colour online) Locations of doublets and enforcement points for conformal mapping of the engine inlet into three slits.

We avoid the use of commercial grid generation packages because such packages are mostly designed to provide unstructured grids, which are not best for computing wave propagation. Also, conformal mapping grids have orthogonal grid lines; this feature generally leads to more accurate finite difference approximations to spatial derivatives.

The engine casing and hub is first extended by symmetry about the vertical line passing through the fan face, as shown in figure 4. Doublets are placed along the centrelines of the three bodies in figure 4. A large set of enforcement points on the surface of the bodies is selected. The strengths of the doublets are then chosen so that the enforcement points are mapped onto three parallel slits in the computational plane, as shown in figure 5. Because the number of enforcement points is much larger

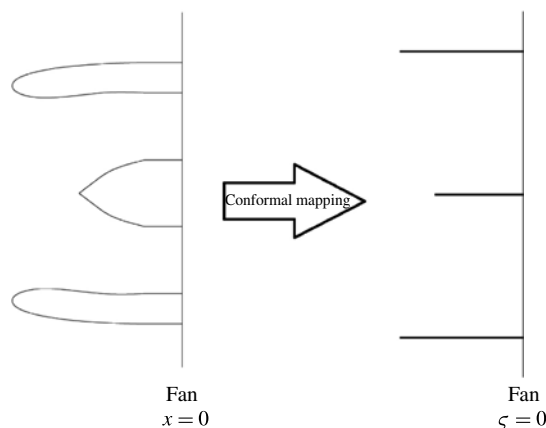
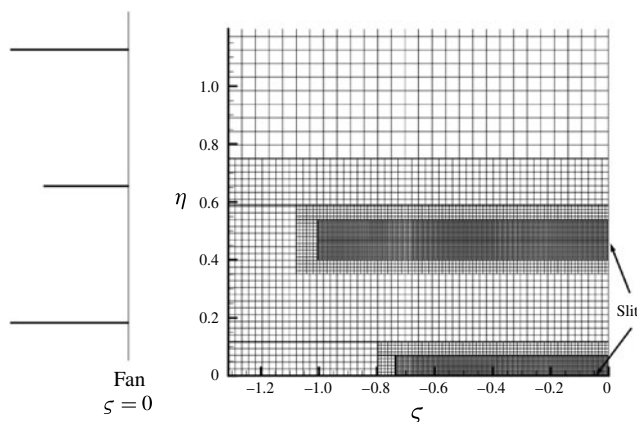


FIGURE 5. Mapping of engine inlet into three slits in the computational domain.

FIGURE 6. Multi-size Cartesian grid in the computational plane or the  $\zeta$ - $\eta$  plane.

than the number of doublets, the number of linear algebraic equations derived from mapping to the slits condition is far higher than the number of unknowns. It is an over-determined system. Such a system can, however, be solved by a mean-least-squared method known as the method of normal matrix. Details of the conformal mapping method are provided in Tam & Ju (2012).

In the mapped plane, i.e. the computational plane or the  $\zeta$ - $\eta$  plane, the inlet consists of three slits. A Cartesian grid can easily be fitted into the three-slits geometry in the computational domain, as shown in figure 6. Because of axisymmetry, only the top half of the inlet needs to be considered. A multiple-size grid is used to ensure accuracy and efficiency. The finest grid is used around the walls of the casing and the hub, as shown in figure 6. In moving outwards from these finest regions, three grid-size changes occur, each increasing the grid size by a factor of two. The result is a total of four grid sizes, where the grid size of the coarsest region is eight times that of the finest region. This grid arrangement is adopted in anticipation of using the multi-size-mesh and multi-time-step dispersion-relation-preserving (DRP) scheme (see Tam & Webb 1993; Tam & Kurbatskii 2003) as the computational algorithm.

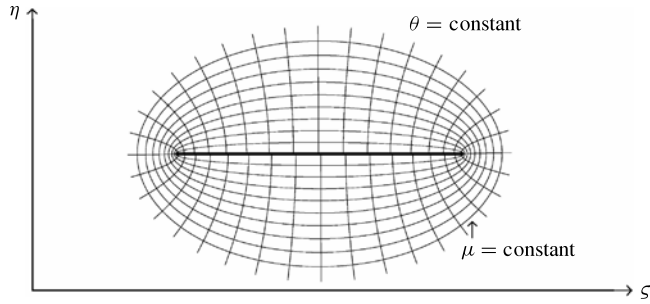


FIGURE 7. Elliptic coordinate lines form a body-fitted grid around a slit.

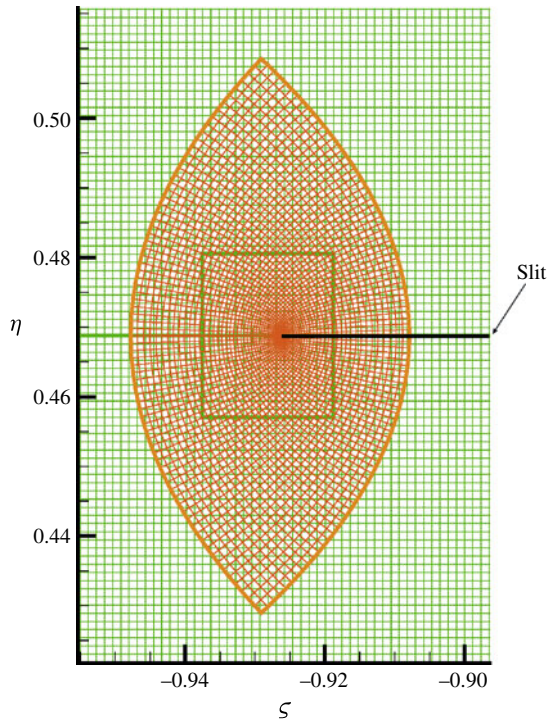


FIGURE 8. (Colour online) A lens-shaped region of the elliptic grid of figure 7 is used to improve the resolution at the tip of a slit.

In the computational domain, both the casing and the hub are mapped into slits. A Cartesian grid would provide adequate resolution everywhere except at the tip of the slit where there is a singularity in the conformal map. To improve resolution near the tips of the slits, an elliptic grid ( $\mu$ – $\theta$  coordinates), which forms a body-fitted grid to a slit, is introduced (see figure 7). A lens-shaped portion of the elliptic grid, which overlaps the singularity of the conformal map, as shown in figure 8, is included in the computation. The Cartesian grid computation ends at the boundary of the rectangular box shown in figure 8. The computation in the elliptic grid is confined to the lens-shaped region in this figure. In the overlapping region, data are transferred by interpolation from one grid to the other, typical of the overset grid method (see Tam & Hu 2004; Tam 2012). In the physical plane, the grid design around the casing and



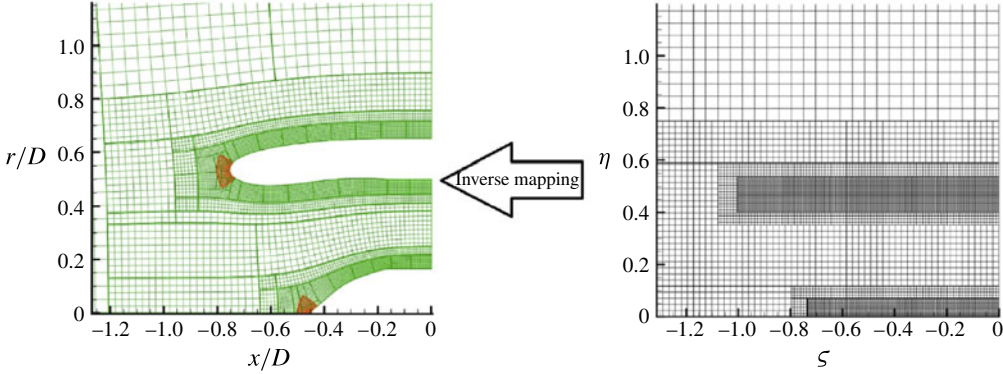


FIGURE 9. (Colour online) Enlarged grid design in the computational and the physical planes.

the hub is shown in figure 9. Note that in figure 9, the grids have been coarsened for illustrative purposes.

## 2.2. Mean flow computation

For our computation, the gas is assumed to be inviscid. The mean flow is axisymmetric, so there is no azimuthal dependence. The governing equations are the Euler equations, which written in the computational coordinates  $(\zeta, \eta)$  in dimensionless form are:

length scale =  $D$  (internal diameter of duct at fan face),  
velocity scale =  $a_0$  (ambient sound speed),  
time scale =  $D/a_0$ ,  
density scale =  $\rho_0$  (ambient gas density),  
pressure scale =  $\rho_0 a_0^2$ ,

$$\begin{aligned} \frac{\partial \rho}{\partial t} + v \left( \frac{\partial \rho}{\partial \zeta} \frac{\partial \zeta}{\partial r} + \frac{\partial \rho}{\partial \eta} \frac{\partial \eta}{\partial r} \right) + u \left( \frac{\partial \rho}{\partial \zeta} \frac{\partial \zeta}{\partial x} + \frac{\partial \rho}{\partial \eta} \frac{\partial \eta}{\partial x} \right) \\ + \rho \left( \frac{\partial v}{\partial \zeta} \frac{\partial \zeta}{\partial r} + \frac{\partial v}{\partial \eta} \frac{\partial \eta}{\partial r} + \frac{v}{r} + \frac{\partial u}{\partial \zeta} \frac{\partial \zeta}{\partial x} + \frac{\partial u}{\partial \eta} \frac{\partial \eta}{\partial x} \right) = 0, \end{aligned} \quad (2.1)$$

$$\begin{aligned} \frac{\partial u}{\partial t} + v \left( \frac{\partial u}{\partial \zeta} \frac{\partial \zeta}{\partial r} + \frac{\partial u}{\partial \eta} \frac{\partial \eta}{\partial r} \right) + u \left( \frac{\partial u}{\partial \zeta} \frac{\partial \zeta}{\partial x} + \frac{\partial u}{\partial \eta} \frac{\partial \eta}{\partial x} \right) \\ + \frac{1}{\rho} \left( \frac{\partial p}{\partial \zeta} \frac{\partial \zeta}{\partial x} + \frac{\partial p}{\partial \eta} \frac{\partial \eta}{\partial x} \right) = 0, \end{aligned} \quad (2.2)$$

$$\begin{aligned} \frac{\partial v}{\partial t} + v \left( \frac{\partial v}{\partial \zeta} \frac{\partial \zeta}{\partial r} + \frac{\partial v}{\partial \eta} \frac{\partial \eta}{\partial r} \right) + u \left( \frac{\partial v}{\partial \zeta} \frac{\partial \zeta}{\partial x} + \frac{\partial v}{\partial \eta} \frac{\partial \eta}{\partial x} \right) \\ + \frac{1}{\rho} \left( \frac{\partial p}{\partial \zeta} \frac{\partial \zeta}{\partial r} + \frac{\partial p}{\partial \eta} \frac{\partial \eta}{\partial r} \right) = 0, \end{aligned} \quad (2.3)$$

$$\begin{aligned} \frac{\partial p}{\partial t} + v \left( \frac{\partial p}{\partial \zeta} \frac{\partial \zeta}{\partial r} + \frac{\partial p}{\partial \eta} \frac{\partial \eta}{\partial r} \right) + u \left( \frac{\partial p}{\partial \zeta} \frac{\partial \zeta}{\partial x} + \frac{\partial p}{\partial \eta} \frac{\partial \eta}{\partial x} \right) \\ + \gamma p \left( \frac{\partial v}{\partial \zeta} \frac{\partial \zeta}{\partial r} + \frac{\partial v}{\partial \eta} \frac{\partial \eta}{\partial r} + \frac{v}{r} + \frac{\partial u}{\partial \zeta} \frac{\partial \zeta}{\partial x} + \frac{\partial u}{\partial \eta} \frac{\partial \eta}{\partial x} \right) = 0, \end{aligned} \quad (2.4)$$



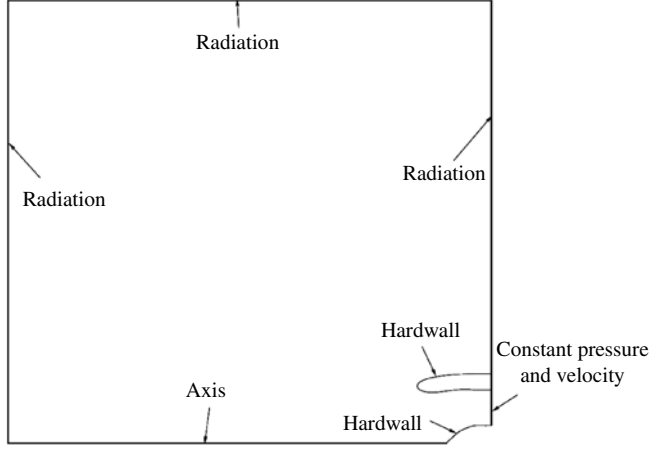


FIGURE 10. Boundary conditions imposed in the numerical simulations of mean flow.

where  $\zeta(x, r)$ ,  $\eta(x, r)$  and inverses  $x(\zeta, \eta)$ ,  $r(\zeta, \eta)$  are given by the conformal mapping function. The variables  $(u, v)$  are the velocity components in the axial and radial directions, respectively.

For computation in the overset elliptic grid, a further change of variables from  $(\zeta, \eta)$  to  $(\mu, \theta)$  is necessary. This step is fairly straightforward, so the governing equations in  $(\mu, \theta)$  coordinates will not be written out.

In addition to the governing equations, boundary conditions are needed to compute the mean flow. The different types of boundary conditions imposed in the present computation are shown in figure 10. The radiation boundary conditions used are the asymptotic radiation boundary conditions developed by Tam & Dong (1996); see also Tam (2012). Because these conditions are derived from asymptotic solutions, the equations implicitly require the specification of a centre of the acoustic source. The radiation boundary conditions may be written as

$$\left[ \frac{1}{V(\theta)} \frac{\partial}{\partial t} + \cos \theta \frac{\partial}{\partial x} + \sin \theta \frac{\partial}{\partial r} + \frac{1}{\sqrt{(x - x_s)^2 + (r - r_s)^2}} \right] \begin{bmatrix} \rho - 1 \\ u - M_{flight} \\ v \\ p - \frac{1}{\gamma} \end{bmatrix} = 0, \quad (2.5)$$

where  $M_{flight}$  is the forward flight Mach number,  $(x_s, r_s)$  are the physical coordinates of the sound source and  $\theta$  is the angle between the positive  $x$ -axis and the line connecting the source point and the boundary point. In addition,  $V(\theta)$ , the asymptotic acoustic wave speed, is given by

$$V(\theta) = [M_{flight}^2 \cos^2 \theta + (1 - M_{flight}^2 \sin^2 \theta)^{1/2}]. \quad (2.6)$$

The acoustic source location to be used for determining angle  $\theta$  in (2.5) and (2.6) is shown in figure 3. For boundary ABC, the origin is at the point O. For boundary CDE, the source is taken to lie along the line segment OM, with the source at point O for boundary point C and the source at point M for boundary point E. For intermediate boundary points along CDE, the source point distance from O along OM is kept

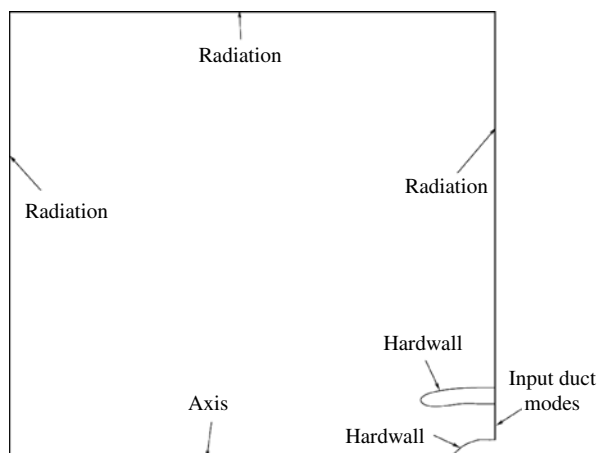


FIGURE 11. Boundary conditions used to compute the acoustic field.

proportional to the boundary point distance from C along CDE. For boundary EF, the origin is taken to be point M.

For the axis boundary condition, the method of Shen & Tam (2002) (see also Tam 2012) is used. This set of boundary conditions avoids the apparent singularity at the axis of the cylindrical coordinates where  $r = 0$ . This axis boundary treatment works well in all the present computations. At the fan face boundary, the desired Mach number is prescribed. The corresponding value of pressure is computed according to conservation of enthalpy and is enforced at the boundary.

### 2.3. Acoustic computation

The acoustic field in the computational domain is governed by the linearized Euler equations. They can be derived easily. For this reason, these equations will not be written out explicitly. The various types of boundary conditions to be imposed on the acoustic field are shown in figure 11. They are nearly the same as those for the mean flow computation. The exception is at the fan face boundary. Here, an incoming duct mode is introduced into the computational domain. For this purpose, the split variable method (see Tam 1998, 2012) is used. To absorb any possible acoustic disturbances reflected back to the fan face from the interior of the computational domain, a perfectly matched layer (PML) absorbing boundary condition is added externally to the computational domain. The PML formulation and implementation follow the work of Hu (2001, 2008). We find computationally that this boundary treatment performs satisfactorily.

All time marching computations in the present investigation are carried out using the multi-size-mesh multi-time-step DRP scheme of Tam & Kurbatskii (2003) (see Tam 2012). The acoustic computation uses the same grid as that for the mean flow computation. This eliminates the necessity of interpolating the mean flow onto the acoustic grid. This scheme has proven to be accurate and efficient.

### 2.4. Acoustic duct modes

It will be assumed that the sound to be radiated out of the engine inlet is from a duct mode of an annular duct with a hub/tip ratio  $\sigma$ . The fan face Mach number and the forward flight Mach number, or wind tunnel Mach number in the case of

simulated forward flight, are denoted by  $M_{fan}$  and  $M_{flight}$ , respectively. For a duct mode with azimuthal mode number  $m$  and radial mode number  $n$ , the dimensionless axial wavenumber  $k_{mn}$  (for simulated forward flight) is (assuming plug flow in duct)

$$k_{mn} = \frac{-\omega u_f - a_f \{\omega^2 - (a_f^2 - u_f^2) \beta_{mn}^2\}^{1/2}}{a_f^2 - u_f^2}, \quad (2.7)$$

where  $\omega$  is the angular frequency, and  $u_f$ ,  $\rho_f$  and  $a_f$  are the dimensionless fan face velocity, density and sound speed, respectively. These are given by

$$u_f = M_{fan} a_f, \quad \rho_f = (a_f)^{2/(\gamma-1)}, \quad a_f = \left[ \frac{1 + \frac{1}{2}(\gamma-1)M_{flight}^2}{1 + \frac{1}{2}(\gamma-1)M_{fan}^2} \right]^{1/2}. \quad (2.8)$$

In the above,  $\beta_{mn}$  is the root of the dispersion relation

$$J'_m \left( \frac{1}{2} \beta_{mn} \right) Y'_m \left( \frac{\sigma}{2} \beta_{mn} \right) - Y'_m \left( \frac{1}{2} \beta_{mn} \right) J'_m \left( \frac{\sigma}{2} \beta_{mn} \right) = 0, \quad (2.9)$$

where  $J_m(\cdot)$  and  $Y_m(\cdot)$  are the Bessel and Neumann functions of order  $m$ . The duct mode eigenfunction is

$$\begin{bmatrix} p_{mn} \\ u_{mn} \\ v_{mn} \\ w_{mn} \\ \rho_{mn} \end{bmatrix} = A_{mn} \begin{bmatrix} 1 \\ k_{mn} \\ \rho_f(\omega - k_{mn}u_f) \\ -i\beta_{mn} \\ \rho_f(\omega - k_{mn}u_f) \\ m \\ \rho_f(\omega - k_{mn}u_f)r \\ \frac{1}{a_f^2} \end{bmatrix} \times \left\{ J_m(\beta_{mn}r) - \frac{J'_m \left( \frac{\sigma}{2} \beta_{mn} \right)}{Y'_m \left( \frac{\sigma}{2} \beta_{mn} \right)} Y_m(\beta_{mn}r) \right\} \exp[i(k_{mn}x + m\varphi - \omega t)]. \quad (2.10)$$

(Note that, in this work, the radial mode number  $n$  is set equal to the total number of maxima and minima of the eigenfunction. According to this numbering system,  $n = 0$  is possible only for the plane wave mode (i.e.  $m = n = 0$ ). For azimuthal modes with  $m \neq 0$ , the lowest-order radial mode is  $n = 1$ .)

Cantrell & Hart (1964) derived an expression for the energy flux in the upstream direction. On following their formula, with fan face variables  $\rho_f$ ,  $u_f$  and  $a_f$ , the energy flux,  $F_{mn}$ , for the  $(m, n)$  duct mode is found to be

$$F_{mn} = \pi Q_{mn} A_{mn}^2 \left\{ [1 + M_{fan}^2] \frac{k_{mn}}{\rho_f(\omega - k_{mn}u_f)} + \frac{u_f}{\rho_f} \left[ \frac{k_{mn}^2}{(\omega - k_{mn}u_f)^2} + \frac{1}{a_f^2} \right] \right\}, \quad (2.11)$$

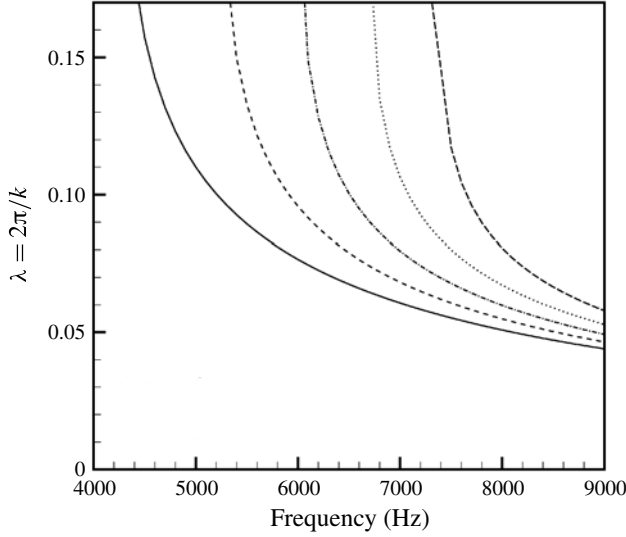


FIGURE 12. Variation of duct mode axial wavelength with frequency;  $M_{fan} = 0.4$ ,  $M_{flight} = 0$ ,  $m = 22$ : —,  $n = 1$ ; ---,  $n = 2$ ; - · -,  $n = 3$ ; ·····,  $n = 4$ ; — — —,  $n = 5$ .

where

$$Q_{mn} = \begin{cases} \frac{1}{8}(1 - \sigma^2), & m = n = 0, \beta_{mn} = 0, \\ \int_{\sigma/2}^{1/2} \left[ J_m(\beta_{mn}r) - \frac{J'_m\left(\beta_{mn}\frac{\sigma}{2}\right)}{Y'_m\left(\beta_{mn}\frac{\sigma}{2}\right)} Y_m(\beta_{mn}r) \right]^2 r dr, & \beta_{mn} \neq 0. \end{cases} \quad (2.12)$$

If PWL is the sound power level of the  $(m, n)$ th duct mode in decibels (dB) and  $W_0 = 10^{-12}$  watts is the reference sound power level for the dB unit, the duct mode amplitude can easily be found to be

$$A_{mn} = \left\{ \frac{W_0 10^{PWL/10}}{\rho_0 a_0^3 D^2 \pi Q_{mn} [1 + M_{fan}^2] \frac{k_{mn}}{\rho_f (\omega - k_{mn} u_f)} + \frac{u_f}{\rho_f} \left[ \frac{k_{mn}^2}{(\omega - k_{mn} u_f)^2} + \frac{1}{a_f^2} \right]} \right\}^{1/2}. \quad (2.13)$$

Of interest later on is the dependence of the axial wavelengths of duct modes on frequency and azimuthal mode number. The axial wavelength of the  $(m, n)$ th mode,  $\lambda_{mn}$ , is related to the axial wavenumber  $k_{mn}$  of (2.7) by  $\lambda_{mn} = 2\pi/k_{mn}$ . Thus, by examining the numerator of (2.7), it is easy to see that, for fixed values of  $M_{fan}$ ,  $M_{flight}$ ,  $m$  and  $n$ , an increase in frequency leads to an increase in  $k_{mn}$  and hence a decrease in wavelength. Figure 12 shows typical examples of the reduction in axial wavelength with increase in frequency.

The eigenvalue  $\beta_{mn}$  of (2.7) is the root of (2.9). It is well known that, for a fixed radial mode number  $n$ , the value of  $\beta_{mn}$  from (2.9) increases with  $m$ . Because of this, it follows from (2.7) that, for fixed  $M_{fan}$ ,  $M_{flight}$ ,  $n$  and frequency  $f$  or  $\omega$ , a decrease in azimuthal mode number  $m$  would lead to an increase in  $k_{mn}$  and, therefore, a reduction in axial wavelength. Figure 13 shows typical examples of the variation of  $\lambda_{mn}$  with  $m$ .

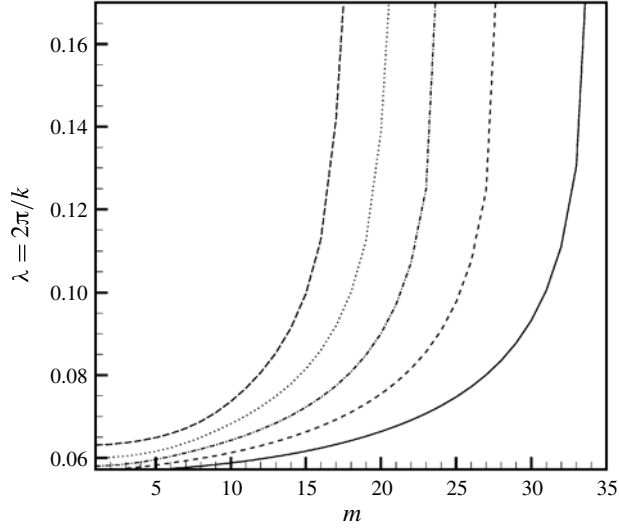


FIGURE 13. Variation of duct mode axial wavelength with azimuthal mode number;  $M_{fan} = 0.4$ ,  $M_{flight} = 0$ ,  $f = 6400$  Hz,  $m = 22$ : —,  $n = 1$ ; ---,  $n = 2$ ; — · —,  $n = 3$ ; ·····,  $n = 4$ ; — — —,  $n = 5$ .

### 2.5. Extension to the far field

A computational domain inevitably has a finite size. To determine far-field directivity, it is, therefore, necessary to extend the numerical solution to the far field. Currently, the Kirchhoff method and the Ffowcs Williams & Hawkings (1969) method (see also Pilon & Lyrntzis 1998; Lyrntzis 2003) are the two most popular methods for extending near-field results to the far field. To use these methods, one encloses the near field by a matching surface. The extension is to continue the information prescribed on the matching surface to the far field. In both the Kirchhoff method and the Ffowcs Williams and Hawkings method, at least three sets of data are required on the matching surface. The data needed are the pressure, the normal gradient of the pressure on the surface and the time derivative of pressure. Recently, Reba *et al.* (2005), Reba, Simonich & Schlunker (2008), Tam, Pastouchenko & Viswanathan (2010) and Tam (2012) have shown that the near-to-far acoustic field extension, or the continuation problem, can also be accomplished by the use of a surface Green's function. For the jet engine inlet duct mode radiation problem, the surface Green's function method proves the simplest to use and to implement. Instead of requiring three sets of data, as the Kirchhoff method and the Ffowcs Williams and Hawkings method, the surface Green's function method requires only one set of data, namely, the value of pressure on the matching surface. For this reason, the surface Green's function method is adopted in this work. The mathematical details of the surface Green's function method for the jet engine inlet noise radiation problem are given in the [Appendix](#).

### 3. Code validation

To validate the computer code developed in this investigation, the JT15D static engine test data are used. Details of this experiment can be found in the papers by Heidelberg *et al.* (1981), Baumeister & Horowitz (1984) and Preisser *et al.* (1985).

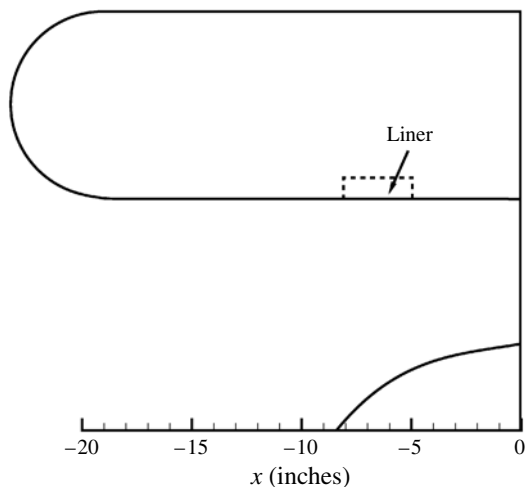


FIGURE 14. Geometry of JT15D engine inlet, including the location of a liner segment.

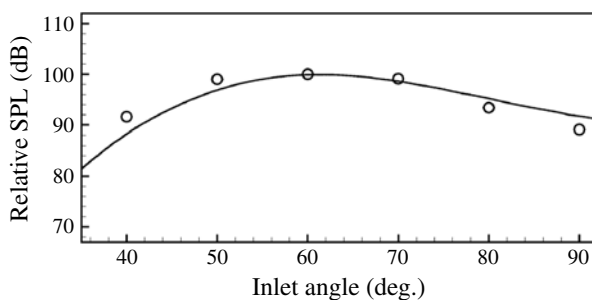


FIGURE 15. Comparison between computed (—) and measured (○) directivity (hard wall). SPL = sound pressure level.

This set of data has been used for code validation by Ozyoruk *et al.* (2004). Figure 14 shows the geometry of the JT15D engine inlet. In the experiment, the inlet was first tested with a hard wall surface. Then a liner segment was inserted in the casing, as shown in figure 14, and the liner configuration was tested for two separate values of impedance. Hence, three sets of experimental data are available for validation.

The fan of the JT15D engine has 28 blades operating at a blade passage frequency of 3150 Hz. The fan face Mach number is 0.147. There are 41 small rods mounted on the casing wall ahead of the fan. The wake shed by the rods is cut by the fan blades, creating strong interaction tones. By design, the inlet geometry and the blade passage frequency support only one propagating mode with  $m = 13$  and  $n = 1$ . With only one propagating mode, the effort to compare numerical results with experimentally measured directivities is greatly simplified.

Figure 15 shows a comparison between the experimentally measured and computed directivities for the hard wall inlet. As can be seen, there is a good overall agreement. The degree of agreement is comparable to that obtained by Ozyoruk *et al.* (2004). Figures 16 and 17 are comparisons of measured and computed relative directivities for the cases where liner is present. In figure 16, the results are shown for a liner

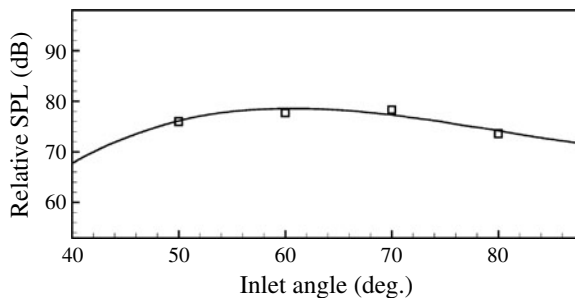


FIGURE 16. Comparison between computed (—) and measured ( $\square$ ) directivity (with liner).  
Liner impedance  $Z = 0.638 + i0.5$ .

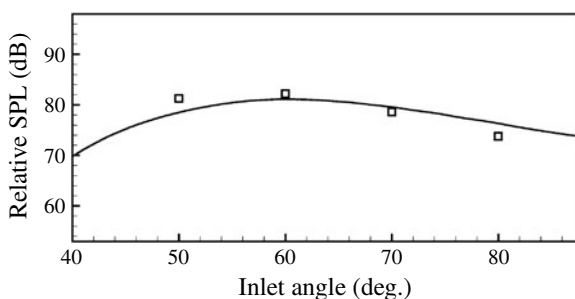


FIGURE 17. Comparison between computed (—) and measured ( $\square$ ) directivity (with liner).  
Liner impedance  $Z = 1.136 + i0.5$ .

with an impedance of  $Z = 0.638 + i0.5$ . Figure 17 shows the comparison for a liner with impedance  $Z = 1.136 + i0.5$ . The agreement is excellent (within experimental uncertainty) for the comparisons shown in figure 16 but somewhat less so for the results of figure 17. Again, the degree of agreement is similar to that obtained by Ozyoruk *et al.* (2004).

#### 4. Mean flow

The mean flow around the inlet of a jet engine changes drastically when there is forward flight. In order to highlight these changes, a typical mean flow computed at static condition will first be presented. This will be followed by a mean flow computed with the same fan face Mach number, but this time at a low forward flight Mach number.

##### 4.1. Mean flow at static condition

Figure 18 shows the streamline pattern around the SDT fan inlet at a fan face Mach number of 0.4. The streamlines are bunched together near the tip of the casing. This indicates that the flow is at a high speed around the casing tip. Figure 19 is an enlarged streamline pattern focusing on the inside of the engine inlet.

Figure 20 plots the tangential velocity,  $V_{\tan}$ , along the casing wall. Figure 20(a) shows the locations of selected points A, B, C, D, E and F along the casing wall. Figure 20(b) provides a plot of the tangential velocity on the casing versus the radial distance from the axis of the inlet. At point A, the flow velocity is practically zero,



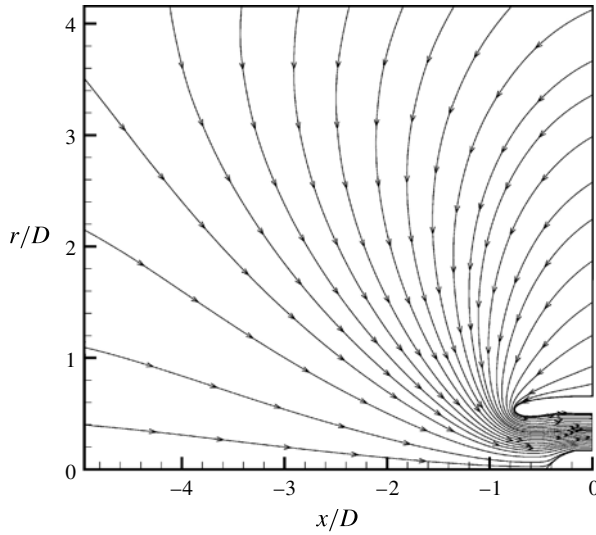


FIGURE 18. Computed streamline pattern at the inlet of the SDT engine at static condition and fan face Mach number 0.4.

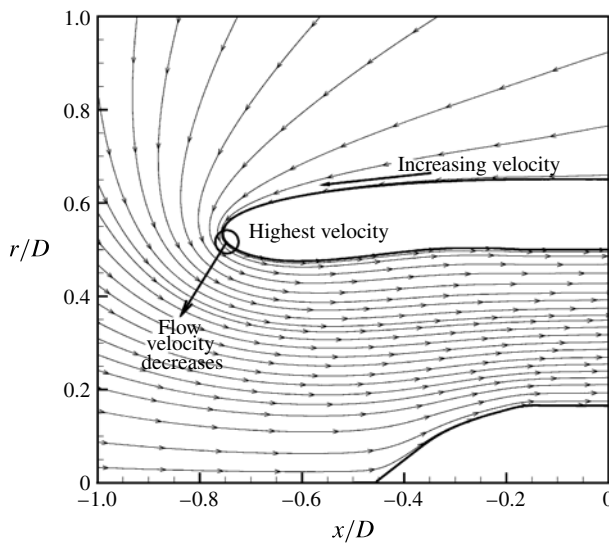


FIGURE 19. Enlarged streamline pattern inside the SDT engine inlet. A strong velocity gradient develops near the lip of the casing. The large arrow points in the direction of negative gradient.

which is the ambient condition. From A to D the flow velocity accelerates quickly to a Mach number of 0.74. This is a transonic Mach number. It is almost twice the fan face Mach number. Along DEF the flow velocity decelerates. It reduces further to Mach 0.4 at the fan face.

Figure 19 shows that the mean flow reaches its highest velocity at the lip of the casing. The flow is slower towards the centre of the inlet. As a result, a significant velocity gradient develops, as indicated in this figure. The velocity gradient points

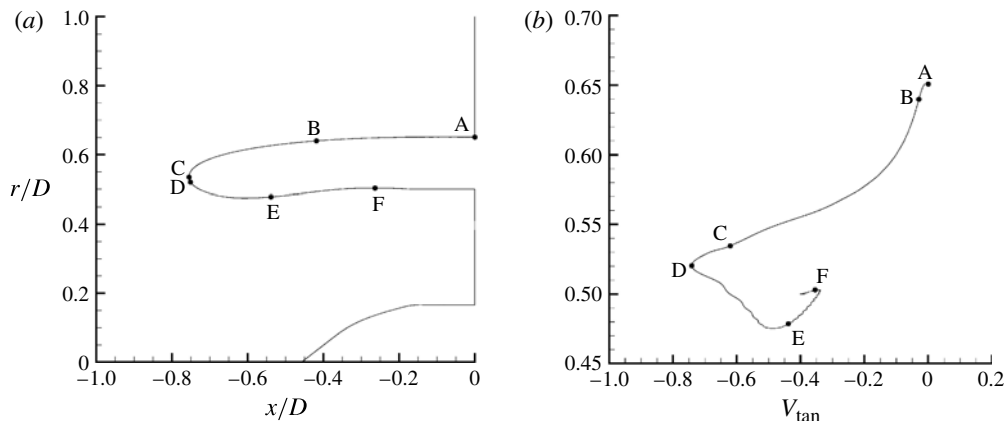


FIGURE 20. (a) Location of points A, B, C, D, E and F on casing. (b) Tangential velocity at points A, B, C, D, E and F.

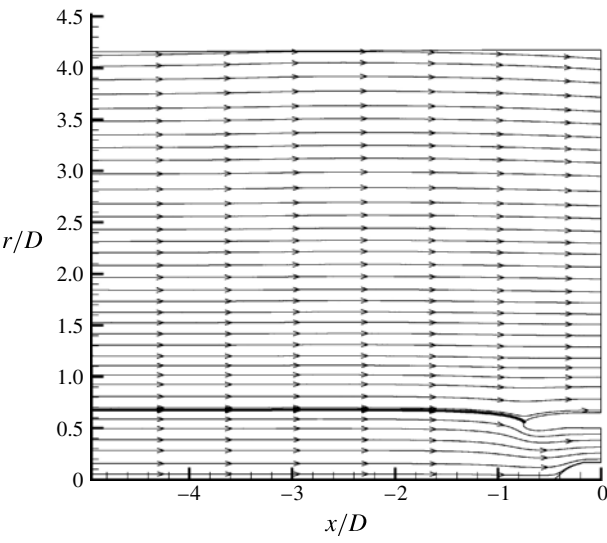


FIGURE 21. Streamline pattern around the SDT engine inlet at fan face Mach number 0.4 and forward flight Mach number 0.2.

towards the lip of the casing, towards the point with the highest velocity. The arrow in this figure points in the direction of negative gradient.

4.2. Mean flow in forward flight

Figure 21 shows the mean flow streamline pattern at the same fan face Mach number as figure 18 but with an added external flow at Mach 0.2. The streamline patterns of the two figures are drastically different. With forward flight, only the flow in a stream tube bounded by the separation streamline is ingested by the engine. The separation streamline is shown as a bold line in this figure. The separation streamline terminates at the lip of the casing. Outside the separation streamline, the fluid simply flows past the engine.

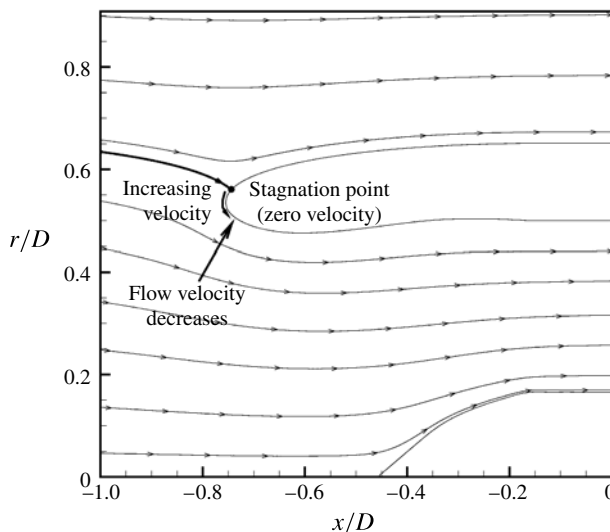


FIGURE 22. Mean velocity gradient developed near the lip of the casing at forward flight Mach number 0.2.

Figure 22 shows an enlarged streamline pattern around the SDT engine inlet. The point at which the separation streamline terminates at the casing lip is a stagnation point. The flow decreases in speed towards the stagnation point. On passing this point on the casing wall, the flow starts to accelerate and ultimately reaches Mach 0.4 at the fan face. Near the lip of the casing, the flow velocity is the lowest at the stagnation point. This creates a velocity gradient pointing away from the casing wall. It is to be noted that the direction of the velocity gradient is opposite in the case with no forward flight, as shown in figure 19. This contrast in the direction of the velocity gradient for static and flight conditions proves to be rather significant, as will be seen in the following section.

## 5. Diffraction and refraction

In this section, duct mode radiation patterns and directivities computed with and without forward flight are presented. The directivities with forward flight are quite different from those without. The reason for this difference will be explained below. Two effects are most important in affecting the direction of radiation: diffraction and refraction. Essentially, the combination of these two effects determines the radiation pattern of a duct mode. Diffraction and refraction are well known in ray acoustics; however, considered here are the propagation of duct modes, not ray acoustics. Duct modes have well-defined and highly organized spatial structures (see the cells in figures 25(b), 45 and 49 in later sections), whereas rays have no internal structure at all. High-speed animations show that each cell of a duct mode propagates as a single unit and does not in any way behave like a ray. Also, due to the spinning of the duct modes, the energy-containing part of each mode is forced to lie close to the duct wall. Thus, the mechanism responsible for causing duct mode diffraction and refraction is not the same as that for rays.

In this work, an inviscid mean flow model is used. In the literature, nearly all published works related to engine inlet radiation use an inviscid model, regardless

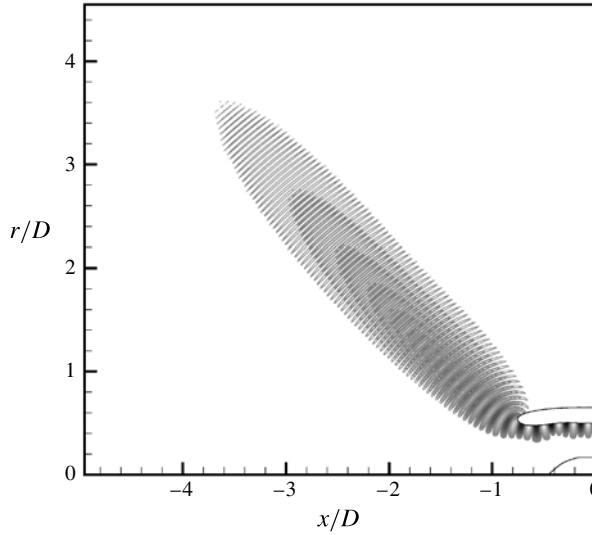


FIGURE 23. Near-field pressure contour pattern showing the dominant direction of radiation. No mean flow. Duct mode with  $m = 22$ ,  $n = 1$ .

of whether an analytical approach is used, such as in the works of Lansing (1970), Homicz & Lordi (1975), Kempton & Smith (1982) and Dougherty (1996), or a computational approach is used, such as in the works of Baumeister & Horowitz (1984), Eversman *et al.* (1985), Roy & Eversman (1995), Ozyoruk & Long (1996), Astley *et al.* (2002), Ozyoruk (2002), Zhang *et al.* (2002), Ozyoruk *et al.* (2004), Premo *et al.* (2007) and Achunche *et al.* (2009). In reality, a viscous/turbulent boundary layer would develop on the surface of the engine casing. Because such a boundary layer could influence the effects of diffraction and refraction on the duct modes, we must assess whether this boundary layer effect can be neglected. To determine this, the parameter  $\delta/\lambda$  is calculated. This is the ratio of the boundary layer thickness  $\delta$  at the tip of the engine casing (where mean flow refraction is expected to be largest) and the duct mode wavelength  $\lambda$ . If this ratio is small, the effect of the boundary layer on the propagation of the duct modes will also be small. To estimate  $\delta$ , the computed mean flow velocity along the casing wall (see figure 20b) and the turbulent boundary layer thickness formula by White (1991) are used. For the NASA SDT engine inlet at a duct mode frequency of 5 kHz (with  $m = 22$ ,  $n = 1$ ),  $\delta/\lambda$  is found to be approximately 0.02 (the engine at static condition, for which  $\delta$  is largest, is used for this estimate). This is sufficiently small, so the use of an inviscid mean flow model should be a good first approximation.

### 5.1. Diffraction

In the context of duct mode radiation, we will define diffraction as the natural tendency of the pressure field of a duct mode to follow a curved solid surface as it propagates. This effect causes the wave field's direction of propagation to make a large turn at the lip of an engine casing. To illustrate this process, consider a duct mode of  $m = 22$ ,  $n = 1$  at a frequency of 6.4 kHz radiating out of the SDT engine inlet. We will first study the case without mean flow. That is, the fan face Mach number is zero. This allows us to investigate the propagation of duct modes along the casing wall without any modification by the mean flow. Figure 23 shows the

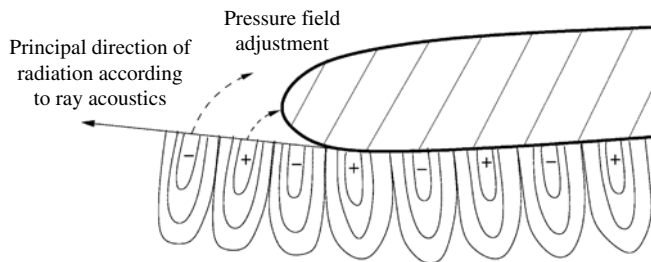


FIGURE 24. A schematic sketch illustrating the complete separation of a duct mode from the casing wall when radiating out of an engine inlet. Required pressure balance prevents this type of complete separation.

radiation pattern. The lines are pressure contours. In this figure, the darkest contour lines represent the highest pressure levels, while the lightest shades of grey represent the lowest pressure levels. The duct mode does not propagate straight out of the inlet in the forward direction. At the casing lip, the sound field turns at an angle of  $\sim 45^\circ$  before radiating away.

Now, a duct mode is made up of alternating high- and low-pressure cells. The highest and the lowest pressure points are adjacent to the wall, as shown in figures 23 and 24. When the sound field propagates along a solid surface, the surface can sustain the high and low pressure variations. Suppose the duct mode propagates in a strictly forward direction, so as to separate from the casing surface as shown in figure 24. In reality, this would not be possible because it would create a pressure imbalance along the line of separation where the ambient pressure is constant. Thus, near the lip of the casing, the pressure field of the duct mode must adjust its pressure distribution by shifting the highest and lowest pressure points away from the wall while it remains attached to the wall, as shown in figure 25(a). This causes the direction of propagation of the duct mode to rotate in the clockwise direction. Figure 25(b) shows a diffraction pattern (pressure contours) at 6400 Hz for a duct mode with  $m = 22$  and  $n = 1$ . The attachment of the sound field to the casing wall is clearly shown even after a  $180^\circ$  turn (see figure 25b).

Diffraction causes the pressure field to rotate in the clockwise direction. As the duct mode turns, the highest and lowest pressure regions gradually move away from the wall. When the highest and lowest pressure regions have detached sufficiently from the wall, the sound field can then radiate away. These processes are observable in a high-speed animation. Thus, the effect of diffraction is what leads the duct mode in figure 23 to radiate predominantly at  $\sim 45^\circ$ .

The effect of diffraction naturally depends on the axial wavelength of the duct mode. For duct modes with short wavelengths, the diffraction effect is small. This should become clear if one considers the limit of very small wavelengths. In this limit, the sound waves are rays, like that of light. If light waves were to radiate out of an engine inlet, they would mostly radiate in the forward direction. In other words, the diffraction effect is absent or minimal. What this reasoning suggests is that the diffraction effect is stronger for long waves and less significant for short waves. A relevant parameter is the ratio of duct mode wavelength to casing wall thickness. Strong diffraction is expected when this ratio is much larger than unity. Figure 26 shows the diffraction pattern of duct modes with  $m = 22$  and  $n = 1$  at a range of frequencies from 5.2 to 7.6 kHz. It is obvious that at low frequencies the

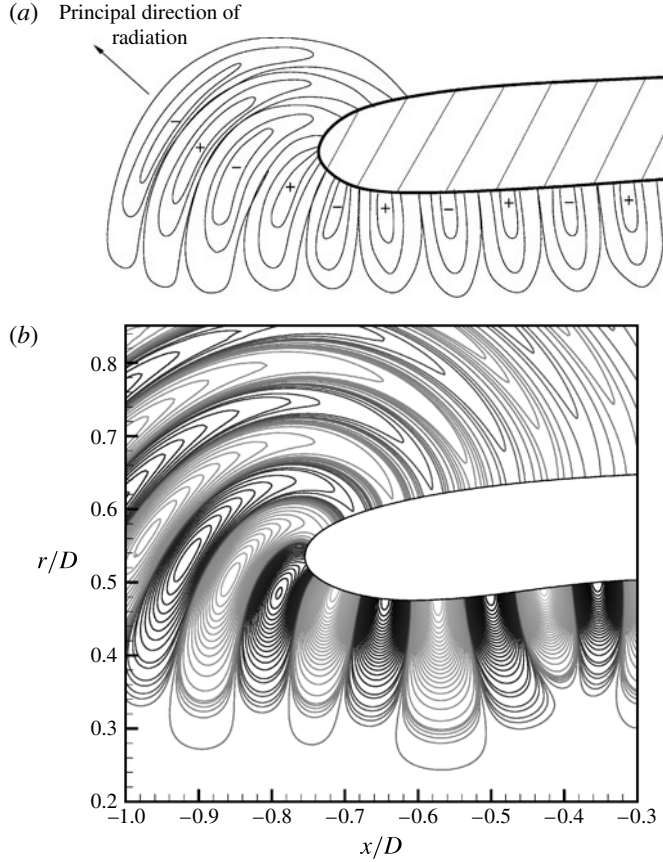


FIGURE 25. (a) To maintain pressure balance, a radiating duct mode must adjust its pressure distribution and remain attached to the casing wall. The adjustment causes the direction of propagation to rotate in the clockwise direction. (b) Instantaneous distribution of pressure contours associated with the radiation of a duct mode with  $m = 22$  and  $n = 1$  at 6400 Hz from the SDT engine inlet. Black represents highest pressure; lightest grey is lowest pressure.

axial wavelength is longer (see figure 12). For these long waves, the turning angle of the direction of radiation (clockwise), measured from the inlet direction, is larger. This is consistent with the above deduction. Figure 27 is a symbolic representation of the dependence of the turning angle on wavelength. In this figure,  $\lambda_1 > \lambda_2 > \lambda_3$  implies decreasing wavelength. The radius of the arc of rotation and the thickness of the arc in the figure represent the relative size of the angle of rotation. The point is this: the shorter the wavelength, the smaller the clockwise turning angle due to diffraction.

### 5.2. Refraction

A jet engine draws in a large quantity of air at its inlet. As discussed in the previous section, this creates a non-uniform mean flow with a significant velocity gradient around the casing lip. At a fan face Mach number of 0.4, in static condition, the mean flow causes the radiation pattern to change from figure 23 to figure 1. Figure 28 is a superposition of the two radiation patterns. It is clear that the presence of a mean flow causes the dominant direction of radiation to rotate in the clockwise direction almost

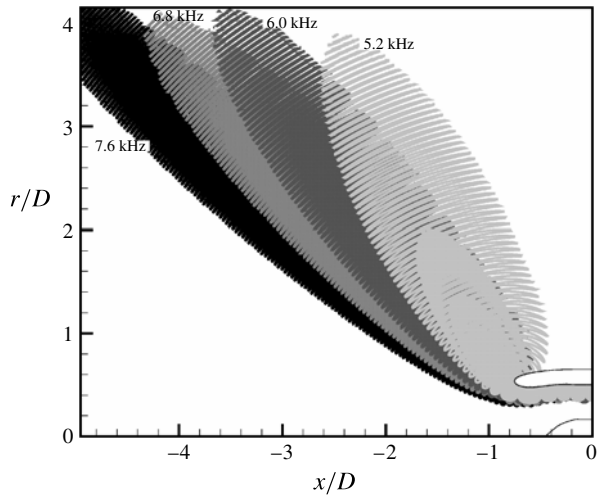


FIGURE 26. Pressure contour patterns showing the radiation of duct modes from the SDT engine inlet (without mean flow) at various frequencies. All duct modes have respective azimuthal and radial mode numbers of  $m = 22$  and  $n = 1$ .

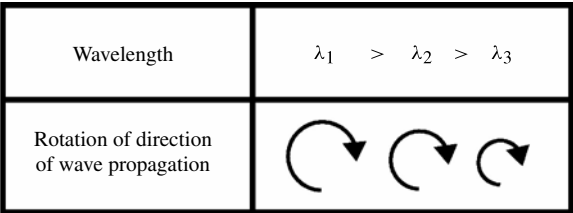


FIGURE 27. Symbolic representation of the dependence of diffraction effect on duct mode wavelength.

an additional 40° past the angle caused by diffraction only. This substantial change in the radiation direction is due to the effect of refraction. At static condition, the velocity gradient near the casing lip is shown in figure 19. Now consider a wave front AA' as shown in figure 29. The wave is propagating against the flow. The flow velocity is highest along the casing wall AB and much slower along streamline A'B'. Thus the propagation speed, equal to the speed of sound minus the flow velocity, is faster along A'B' than along AB. As a result, the wave front will rotate in the clockwise direction. This turns the direction of radiation farther to the right, resulting in an almost 80° direction of propagation (inlet angle).

For a jet engine in forward flight, the effect of refraction is quite different. Figure 30 shows the radiation pattern for three mean flow conditions: zero mean flow, static condition and flight condition. When there is no mean flow, the diffraction effect rotates the dominant direction of radiation to ~45°. In the presence of a mean flow at static condition, refraction further rotates the dominant direction of radiation clockwise to nearly 80°. However, with a forward flight Mach number of 0.2, the refraction effect rotates the dominant direction of radiation by ~10° *counterclockwise* from the angle caused by diffraction only. This counterclockwise rotation is not difficult to



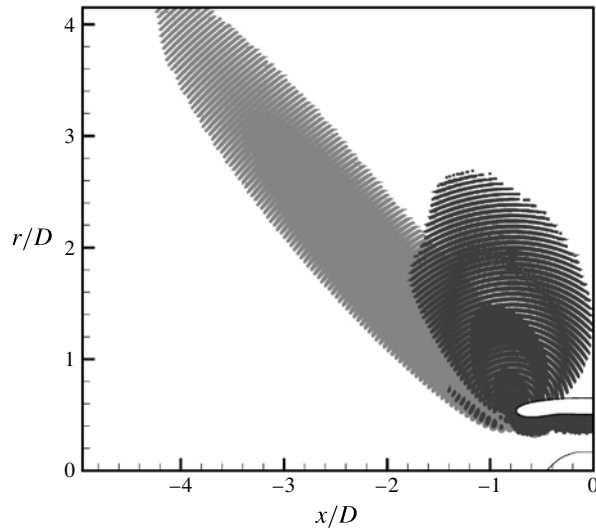


FIGURE 28. Pressure contours showing the change in the dominant direction of radiation when the fan face Mach number increases from zero (no mean flow, light grey) to 0.4 at static condition (dark grey);  $m = 22$ ,  $n = 1$ ,  $f = 6400$  Hz.

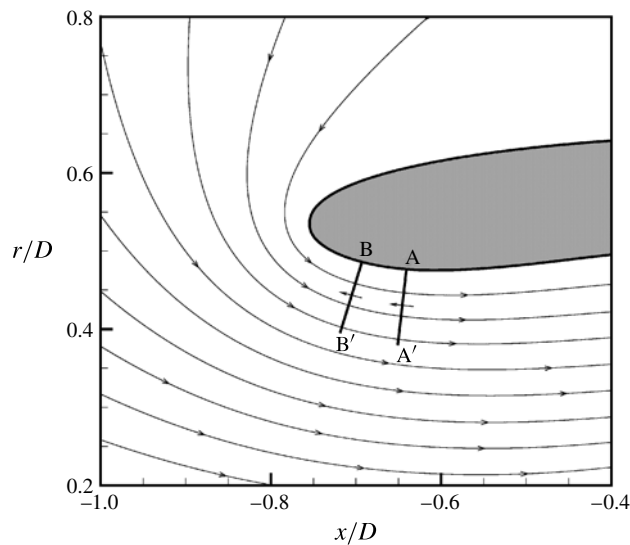


FIGURE 29. Propagation of wave fronts  $AA'$  and  $BB'$  along the casing wall at static condition. The wave front rotates in the clockwise direction upon encountering gradients in the mean flow velocity. This is the refraction effect.

understand. With forward flight, the mean flow pattern and velocity gradients are shown in figure 22. The velocity gradient is almost in the opposite direction to that in the static case (see figure 19). However, the gradient is milder and occurs over a shorter distance along the casing wall. Again, consider the wave fronts  $AA'$  and  $BB'$  as shown in figure 31. This time the flow velocity along the casing lip, i.e.  $AB$ , is slower than that along  $A'B'$ . As a result, the wave front propagates faster along

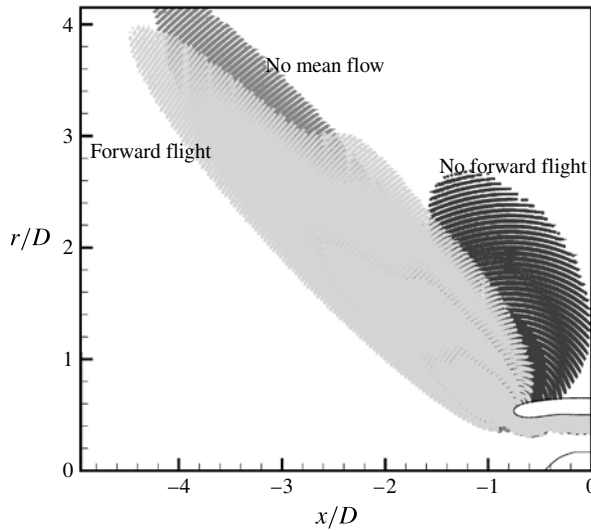


FIGURE 30. Pressure contours showing the dominant direction of radiation when there is no mean flow (medium grey), when there is a mean flow at static condition (dark grey; fan face Mach number 0.4) and when there is forward flight at Mach 0.2 (light grey);  $m = 22$ ,  $n = 1$  and  $f = 6400$  Hz.

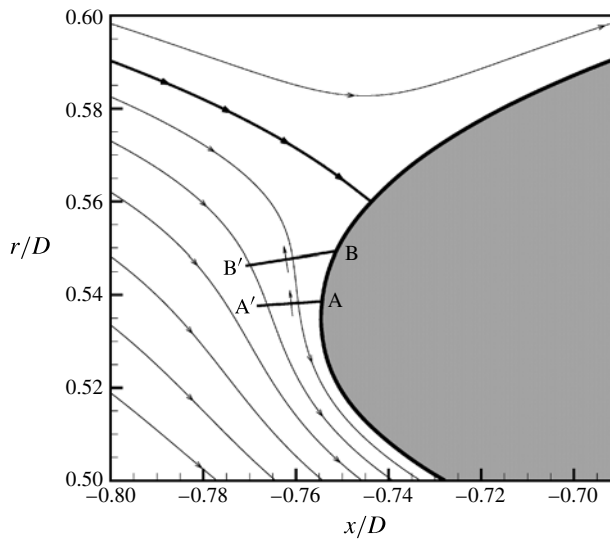


FIGURE 31. Propagation of wave fronts AA' and BB' when there is a Mach 0.2 forward flight. Here, refraction causes a counterclockwise rotation in propagation.

AB than A'B'. This causes a counterclockwise rotation in the direction of wave propagation. This explains the counterclockwise rotation of the dominant direction of radiation for a jet engine in forward flight compared to the case of no mean flow, as observed in figure 30. It is to be noted for forward flight condition that the combined effect of diffraction and refraction still results in an overall clockwise rotation in the propagation direction of waves exiting the inlet. This indicates that the diffraction effect is the more dominant process.

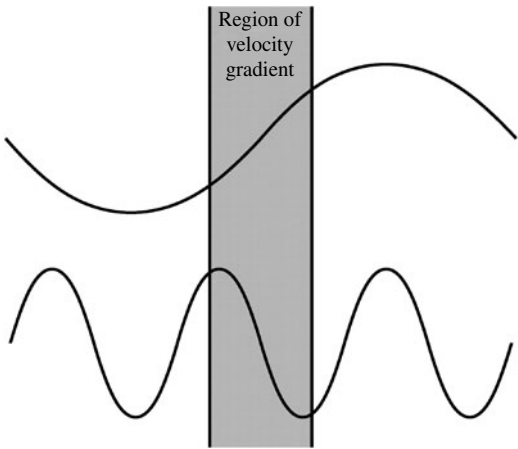


FIGURE 32. Schematic diagram of the propagation of a long and a short wave through a localized region of velocity gradient.



|   |  |        |
|---|--|--------|
| Wavelength                                | $\lambda_1 > \lambda_2 > \lambda_3$  |        |
| Rotation of direction of wave propagation |   | Static |
|   |  | Flight |

FIGURE 33. Symbolic representation of dependence of refraction effect on wavelength. Size of arc indicates the magnitude of rotation due to velocity gradient.

Just as for diffraction, the effect of refraction is also dependent on the duct mode axial wavelength. Figure 32 illustrates the propagation of a long wave and a short wave through a region with a localized velocity gradient. Relative to the long wave, the region is small and hence its effect on the wave is minimal. Relative to the short wave, the non-uniform flow region is quite large; thus, the velocity gradient effect is more significant. Another way of reaching the same conclusion is to consider the limit of wavelength  $\lambda \gg$  length of velocity gradient region. In this limit, the long wave effectively does not see the velocity gradient and hence should experience little effect. On the other hand, for waves with wavelengths much shorter than the size of the non-uniform velocity region, one expects the wave to experience the full strength of refraction when traversing the region. Thus, the direction of propagation of short waves would be severely turned by refraction, whereas long waves would not be much affected. This observation is summarized symbolically in figure 33. In this figure, the case of an engine in static condition is considered separately from the same engine in flight. This is because, in static condition, refraction causes the wave propagation direction to rotate in the clockwise direction, while for an engine in forward flight, the refraction effect causes a counterclockwise rotation in the direction of propagation. In both cases, the angle of rotation increases with a decrease in axial wavelength.

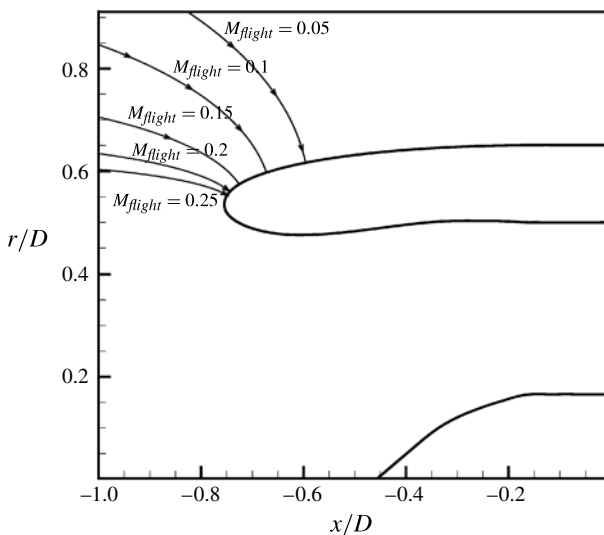


FIGURE 34. Change in the location of stagnation point as forward flight Mach number increases.

## 6. Parametric study of acoustic radiation

We have seen that forward flight has a significant impact on duct mode radiation patterns and directivity. A duct mode is characterized by its azimuthal mode number, radial mode number and frequency. In this section, the results of a parametric study of the effects of forward flight Mach number, frequency and mode numbers are presented.

### 6.1. Forward flight effect

The mean flow around an engine inlet changes with forward flight Mach number. Figure 34 shows the separation streamlines and stagnation point locations for forward flight Mach numbers 0.05, 0.1, 0.15, 0.2 and 0.25. This figure shows that, as flight Mach number increases, the location of the stagnation point on the casing lip becomes somewhat insensitive to further increase after  $M_{flight}$  exceeds 0.15. Figure 35 is similar to figure 20(b). It shows the change in flow velocity on the surface of the casing as flight Mach number increases. At zero forward flight Mach number, the velocity on the surface of the casing can speed up to transonic. But for higher flight Mach numbers, the maximum surface velocity is about the same as that at the fan face. This means that the refraction effect diminishes at high flight Mach numbers.

The effect of forward flight Mach number on directivity is illustrated in figure 36. It is clear that there is a saturation effect, namely, beyond flight Mach number 0.15 there is no substantial change in the directivity. A more simplistic way to see this is to look at the direction of maximum radiation. This is shown in figure 37. This saturation effect on the impact of increasing flight Mach number occurs because the mean flow undergoes only minor changes in response to such increase beyond 0.15, as was shown in figures 34 and 35. Any further refraction effect is minimal, leading to little change in directivity.

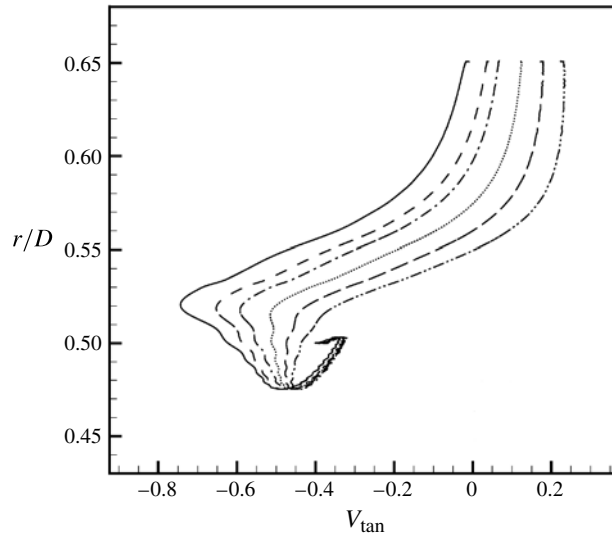


FIGURE 35. Changes in tangential velocity on engine inlet casing wall as forward flight Mach number increases: —,  $M_{flight} = 0.0$ ; ---,  $M_{flight} = 0.05$ ; - · - · -,  $M_{flight} = 0.1$ ; · · · · ·,  $M_{flight} = 0.15$ ; — — —,  $M_{flight} = 0.2$ ; - · - · - · -,  $M_{flight} = 0.25$ .

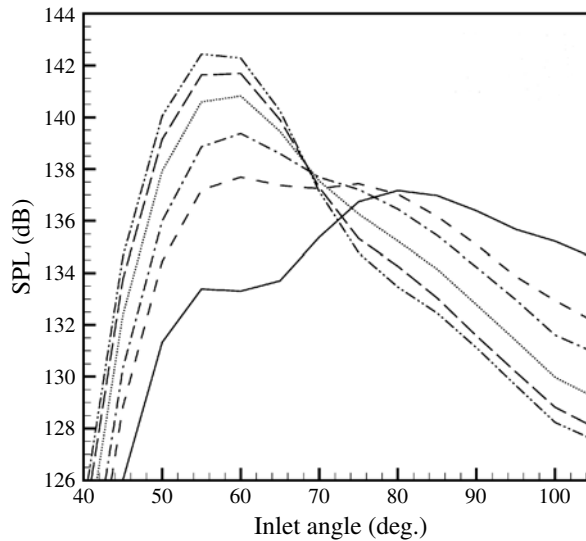


FIGURE 36. Directivity of the radiation of duct mode  $m = 22$ ,  $n = 1$ ,  $f = 5600$  Hz (fan face Mach number 0.4) at varying forward flight Mach numbers: —,  $M_{flight} = 0.0$ ; ---,  $M_{flight} = 0.05$ ; - · - · -,  $M_{flight} = 0.1$ ; · · · · ·,  $M_{flight} = 0.15$ ; — — —,  $M_{flight} = 0.2$ ; - · - · - · -,  $M_{flight} = 0.25$ .

## 6.2. Frequency variation

The axial wavelength of a duct mode changes with frequency. Figure 12 shows the dependence of the duct mode axial wavelength on frequency for the case  $M_{fan} = 0.4$  at static condition. As discussed before, both diffraction and refraction effects are axial-wavelength-dependent. To investigate the dependence of the directivity of radiation

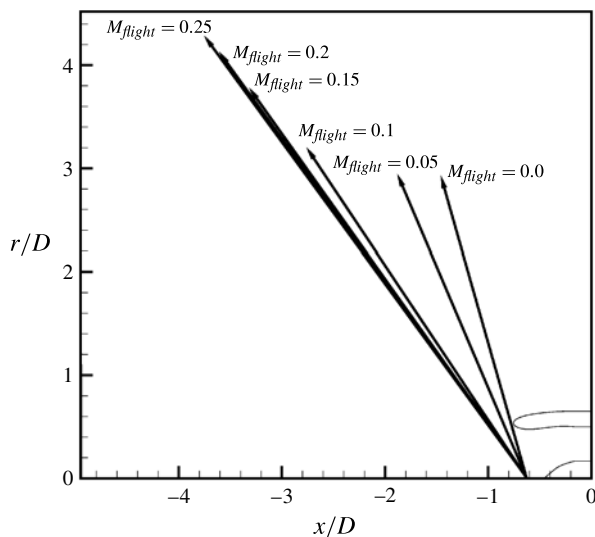


FIGURE 37. Direction of maximum sound radiation at varying forward flight Mach numbers. Duct mode with  $m = 22$ ,  $n = 1$ ,  $f = 5600$  Hz and fan face Mach number 0.4.

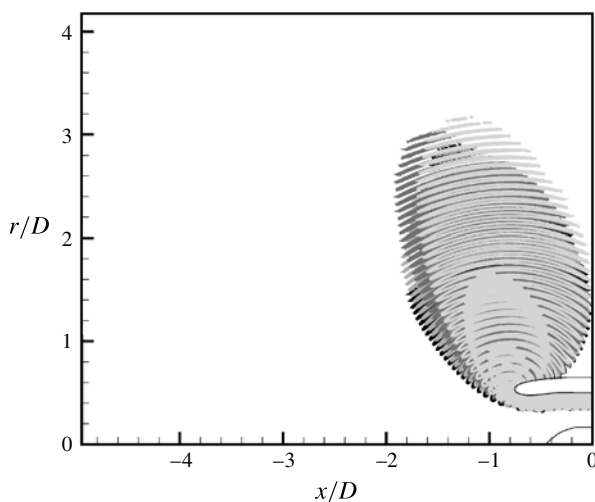


FIGURE 38. Pressure contour pattern of duct mode radiation;  $M_{fan} = 0.4$ ,  $M_{flight} = 0$ ,  $m = 22$ ,  $n = 1$ , with frequencies varying over  $f = 4.5, 4.8, 5.4, 5.6$  and  $6.4$  kHz (see figure 39 for correlation between shades of grey and frequency).

on frequency, we will consider the case  $M_{fan} = 0.4$ ,  $m = 22$  and  $n = 1$ . Figure 38 shows the pressure contour patterns at static condition, i.e.  $M_{flight} = 0$ , when the duct mode frequency varies from 4.5 to 6.4 kHz. It is clear from this figure that the pattern changes only slightly with frequency. Now, let us consider the case at forward flight Mach number 0.2. The pressure contour patterns are displayed in figure 39. At  $M_{flight} = 0.2$ , the dominant direction of radiation is a strong function of frequency. Higher-frequency duct modes radiate at lower inlet angles. Thus, there is a significant difference in the radiation pattern with and without forward flight. This

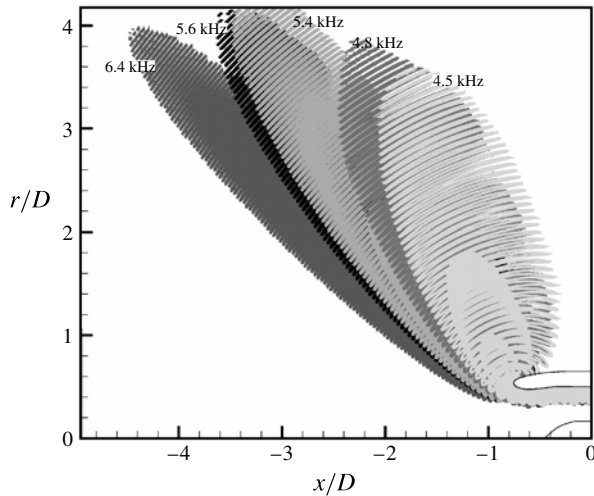


FIGURE 39. Pressure contour pattern of duct mode radiation;  $M_{fan} = 0.4$ ,  $M_{flight} = 0.2$ ,  $m = 22$ ,  $n = 1$ , with frequencies varying over  $f = 4.5, 4.8, 5.4, 5.6$  and  $6.4$  kHz.

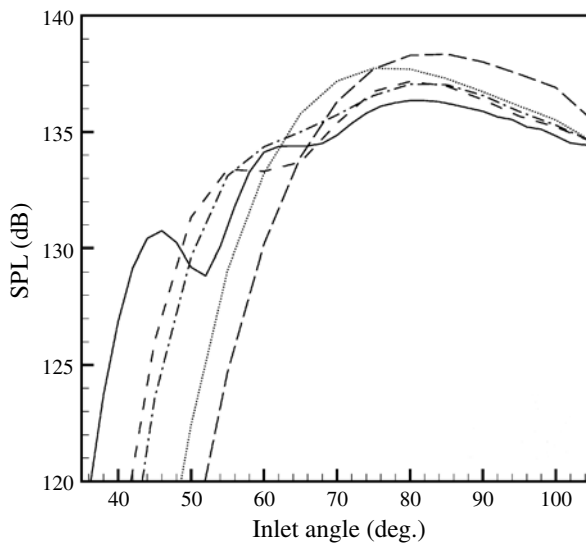


FIGURE 40. Directivities of duct mode radiation;  $M_{fan} = 0.4$ ,  $M_{flight} = 0$ ,  $m = 22$ ,  $n = 1$ : —, 6.4 kHz; ---, 5.6 kHz; - · - · -, 5.4 kHz; · · · · ·, 4.8 kHz; — — —, 4.5 kHz.

phenomenon may also be observed by considering directivity. The directivities are shown in figure 40 for  $M_{flight} = 0$  and in figure 41 for  $M_{flight} = 0.2$ . Again, there is little frequency dependence at the static condition, but a significant dependence exists for an engine in forward flight.

This frequency-dependence phenomenon can be explained by recalling the dependence of the effects of diffraction and refraction on the axial wavelength of duct modes, discussed in §§ 5.1 and 5.2. It is to be noted that duct mode axial wavelengths are shorter at higher frequencies. Thus, the diffraction effect has less impact on high-frequency duct modes, but these high-frequency modes are subjected



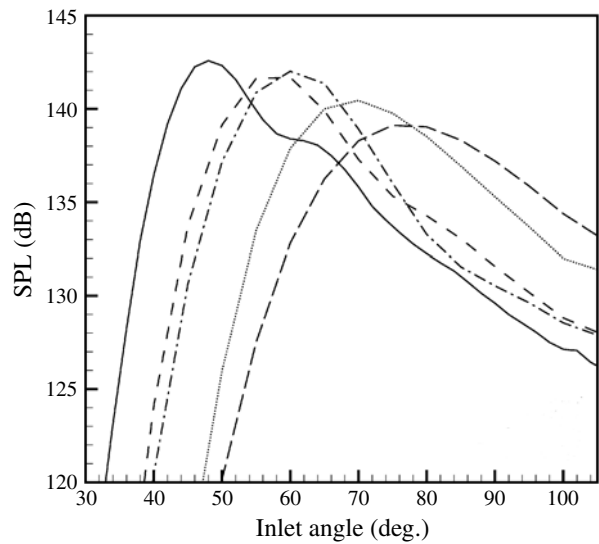


FIGURE 41. Directivities of duct mode radiation;  $M_{fan} = 0.4$ ,  $M_{flight} = 0.2$ ,  $m = 22$ ,  $n = 1$ : —, 6.4 kHz; ---, 5.6 kHz; - · - · -, 5.4 kHz; · · · · ·, 4.8 kHz; — — —, 4.5 kHz.

|             | Static                              | Flight                              |
|-------------|-------------------------------------|-------------------------------------|
| Wavelength  | $\lambda_1 > \lambda_2 > \lambda_3$ | $\lambda_1 > \lambda_2 > \lambda_3$ |
| Diffraction |                                     |                                     |
| Refraction  |                                     |                                     |
| Combined    |                                     |                                     |

FIGURE 42. Symbolic representation of the independent and combined effects of diffraction and refraction with and without forward flight. Size and thickness of circular arc indicate the relative magnitude of the turning angle.

to a stronger refraction effect. On the other hand, for low-frequency duct modes with longer wavelengths, the diffraction effect is larger and refraction effect smaller. At static condition, both effects cause clockwise rotation of the direction of radiation. As a result, the combined effects lead to nearly the same amount of total rotation in the direction of radiation, regardless of wave frequency, as in figure 38. This is shown symbolically in the column labelled ‘Static’ in figure 42. When the engine is in forward flight, the combined effect is different. This is because the refraction effect now turns the direction of radiation counterclockwise, opposite to the effect of diffraction. For low-frequency long waves, the clockwise turning by diffraction is large, and the counterclockwise turning by refraction is small. Alternatively, for

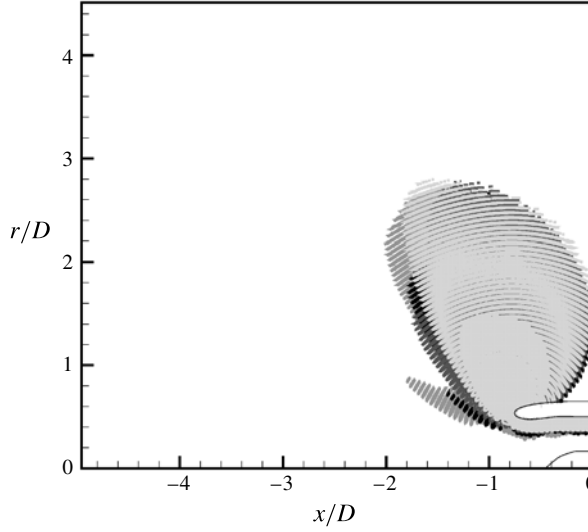


FIGURE 43. Pressure contour patterns associated with duct mode radiation from the SDT engine inlet;  $M_{fan} = 0.4$ ,  $M_{flight} = 0$ ,  $n = 1$ ,  $f = 6400$  Hz and  $m = 18, 22, 26, 30$  (see figure 44 for correlation between shades of grey and azimuthal mode number  $m$ ).

high-frequency short waves, the clockwise turning by diffraction is small, while the counterclockwise turning by refraction is relatively large. The combined result is that low-frequency long waves radiate at a larger inlet angle, while high-frequency short waves radiate at a lower inlet angle, as in figure 39. This is illustrated symbolically in the ‘Flight’ column of figure 42.

### 6.3. Azimuthal mode number variation

At a fixed frequency and radial mode number, the axial wavelength of an upstream-propagating duct mode decreases with a decrease in azimuthal mode number. Figure 13 shows the case of  $M_{fan} = 0.4$ ,  $M_{flight} = 0$ ,  $n = 1$  and  $f = 6400$  Hz for the SDT engine inlet. Thus, it is expected that a variation in azimuthal mode order would have a similar effect on the radiation directivity as the effect of frequency variation. Figure 43 shows the pressure contour patterns of radiation for the cases with  $M_{fan} = 0.4$ ,  $M_{flight} = 0$ ,  $n = 1$ ,  $f = 6400$  Hz and  $m = 18, 22, 26$  and  $30$ . The results suggest that, at static condition, there is little change in the dominant direction of radiation. Figure 44 is the same as figure 43, except with  $M_{flight}$  equal to  $0.2$ . Now there is a spread of the dominant direction of radiation for varying values of  $m$ . The observed azimuthal mode number effect is similar to that due to frequency variation. In fact, just as for frequency variation, the observed phenomenon for variation in azimuthal mode number is caused by the dependence of diffraction and refraction effects on wavelength. Lowering the azimuthal mode number leads to a reduction in axial wavelength. This is equivalent to an increase in wave frequency. So the explanation for frequency dependence also applies to azimuthal mode number dependence.

### 6.4. High-order radial modes

Radial mode number  $n$  (as defined in this investigation) is the sum of the total number of maxima and minima of the duct mode eigenfunction. Because a wave oscillates in

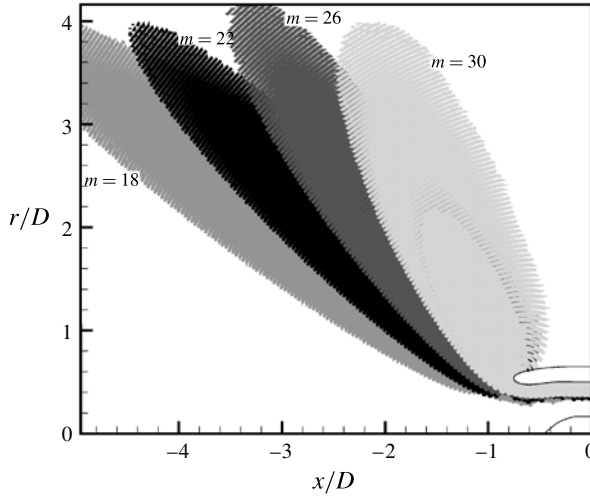


FIGURE 44. Pressure contour patterns associated with duct mode radiation from the SDT engine inlet;  $M_{fan} = 0.4$ ,  $M_{flight} = 0.2$ ,  $n = 1$ ,  $f = 6400$  Hz and  $m = 18, 22, 26, 30$ .

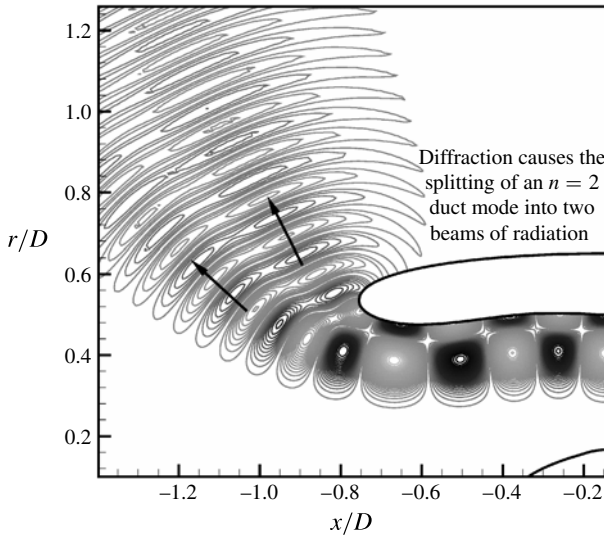


FIGURE 45. Near-field pressure contours showing the splitting of an  $n = 2$  duct mode into two beams;  $M_{fan} = 0.0$ ,  $M_{flight} = 0.0$ ,  $m = 22$ ,  $n = 2$  and  $f = 6400$  Hz. Black represents the highest pressure, and lightest grey is low pressure.

time, a duct mode with radial mode number  $n$  will have a wave field with  $n$  rows of pressure maxima and minima. The high- and low-pressure regions alternate in a staggered pattern (see figure 45). Figure 45 shows the pressure field contour pattern of the  $n = 2$  duct mode at  $M_{fan} = 0.0$ ,  $M_{flight} = 0.0$ ,  $m = 22$  and  $f = 6400$  Hz. Notice that there are two rows ( $n = 2$ ) of alternating high- and low-pressure regions. As diffraction causes the wave field to follow the turn of the casing lip, it is seen that the duct mode splits into two beams. Apparently, the cause of this beam splitting is that the row of pressure maxima and minima adjacent to the wall is influenced more by diffraction.

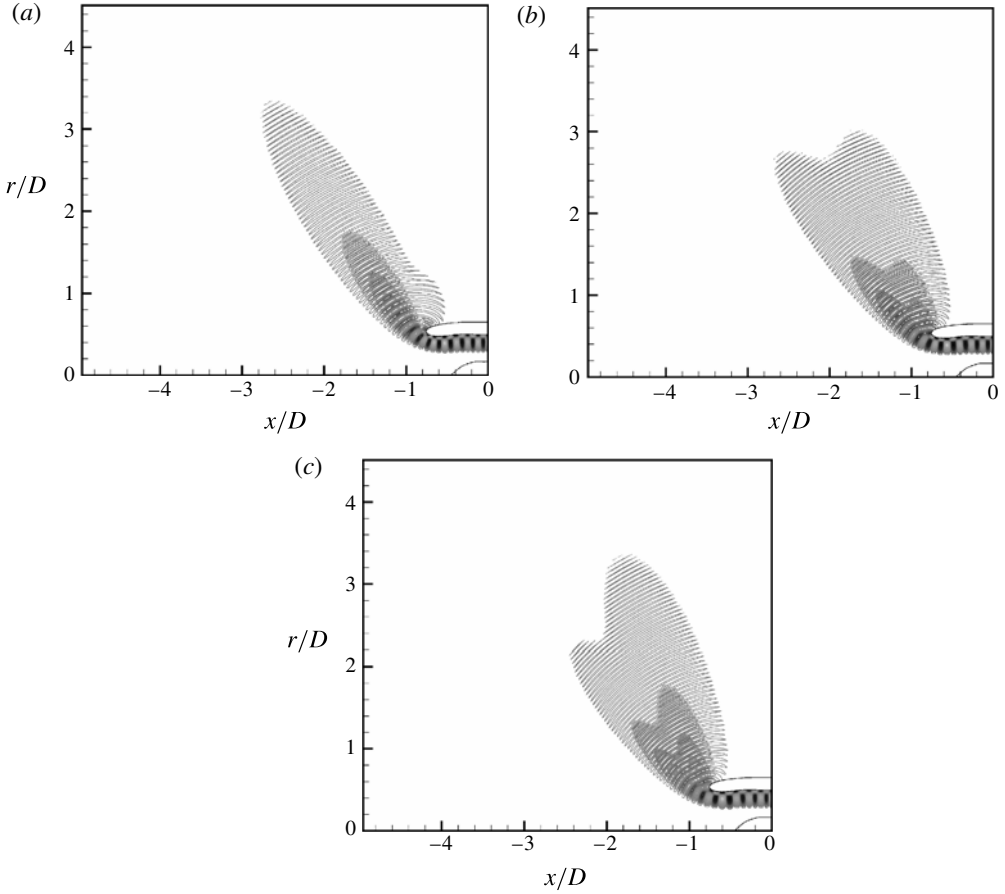


FIGURE 46. Radiation patterns of an  $n = 2$  duct mode with  $m = 22$ ,  $M_{fan} = 0.4$  and  $f = 5600$  Hz for: (a)  $M_{flight} = 0.0$ , (b)  $M_{flight} = 0.15$  and (c)  $M_{flight} = 0.25$ .

Thus, it turns clockwise more than the second row of pressure maxima and minima farther from the wall.

This beam-splitting phenomenon for the second radial mode is affected by forward flight Mach number. Figure 46(a–c) shows the change in the pressure contour pattern for the case  $M_{fan} = 0.4$ ,  $m = 22$  and  $f = 5600$  Hz as flight Mach number increases. Figure 46(a) corresponds to  $M_{flight} = 0.0$ ; figure 46(b) is for  $M_{flight} = 0.15$ ; and figure 46(c) for  $M_{flight} = 0.25$ . Comparing these figures, it is clear that forward flight has a significant influence on the radiation pattern and directivity. Figure 47 is a directivity plot for  $M_{flight} = 0.05, 0.1, 0.15, 0.2$  and  $0.25$ . There are basically two beams of radiation observed for each case of  $M_{flight}$ . As flight Mach number increases, there is a gradual changeover in the dominance of the two beams. At low flight Mach numbers, the beam radiated to the lower inlet angle is the dominant beam. As  $M_{flight}$  increases, a gradual shift in dominance takes place. By  $M_{flight} = 0.15$ , the shift is nearly complete. Beyond 0.15, the beam that radiates to the higher inlet angle is the dominant beam.

Figure 48 shows the results of taking an even higher radial mode number:  $M_{fan} = 0.4$ ,  $M_{flight} = 0.2$ ,  $m = 22$ ,  $n = 4$  and  $f = 6800$  Hz. Upon radiating out of

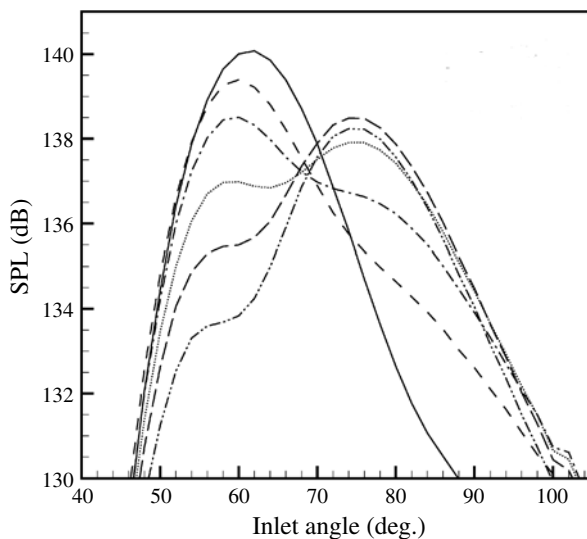


FIGURE 47. Directivity of sound in the far field radiated by an  $n = 2$  duct mode with  $m = 22$ ,  $M_{fan} = 0.4$  and  $f = 5600$  Hz: —,  $M_{flight} = 0.0$ ; ---,  $M_{flight} = 0.05$ ; - · - · -,  $M_{flight} = 0.1$ ; · · · · ·,  $M_{flight} = 0.15$ ; — — —,  $M_{flight} = 0.2$ ; — · · — · ·,  $M_{flight} = 0.25$ .

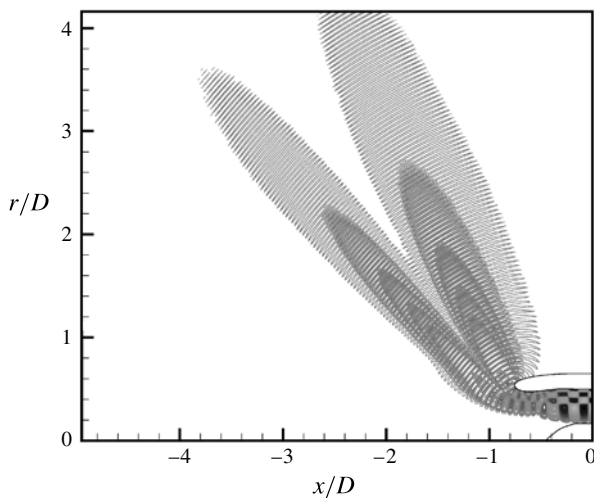


FIGURE 48. Radiation pattern of an  $n = 4$  duct mode with  $m = 22$ ,  $M_{fan} = 0.4$ ,  $M_{flight} = 0.2$  and  $f = 6800$  Hz. The four rows of high- and low-pressure fluctuations near the fan face eventually radiate out of the inlet as two beams.

the engine inlet, the four rows of high- and low-pressure regions merge into two beams. It is to be noted that the radial mode number  $n$  is meaningful inside the duct and in the part of the inlet close to the fan face. Once the sound waves exit the inlet, the radial mode number is no longer meaningful. Therefore, in the engine inlet, there is a region in which a high-order radial mode would undergo a transformation whereby the multi-layer pressure field structure combines into a single sinusoidal spatial structure typical of far-field-propagating acoustic waves. In addition, inside an

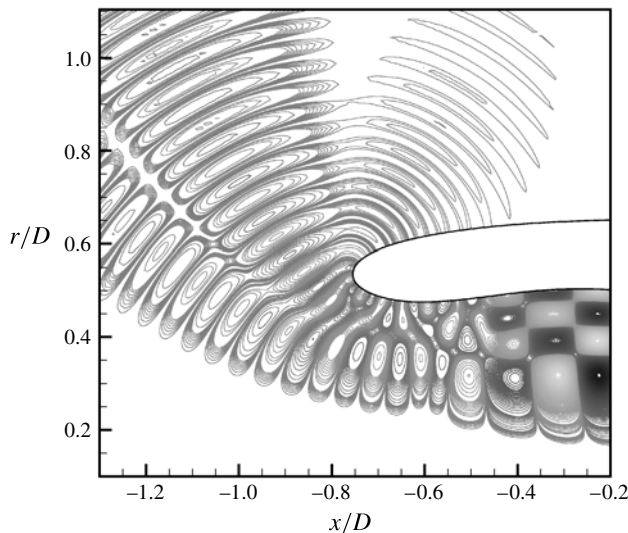


FIGURE 49. Pressure contours showing the transition region at the inlet of an engine for an  $n = 4$  duct mode with  $m = 22$ ,  $M_{fan} = 0.4$ ,  $M_{flight} = 0.0$  and  $f = 6800$  Hz.

engine inlet, the sound field of a duct mode has an axial wavelength determined by frequency, azimuthal mode number, mean flow Mach number and the diameter of the duct. But once the sound field exits the inlet, the wavelength of the freely propagating acoustic wave depends solely on its frequency. Therefore, there is also an adjustment of wavelength in the transition region. This wavelength transition also applies to duct modes with  $n = 1$  radial mode number. Figure 49 shows the transition for an  $n = 4$  duct mode in the engine inlet.

## 7. Summary and conclusion

Numerical simulation of duct mode radiation from a jet engine inlet is carried out. An advanced CAA time marching algorithm and high-quality numerical boundary conditions are used. The computational code is validated by comparing predicted directivities for the JT15D engine with experimental measurements.

Computed results are used to highlight the important physical processes that affect the sound radiation pattern and directivity. It is demonstrated that the phenomena of diffraction and refraction play a key role in determining the ultimate direction of duct mode radiation. Diffraction is the natural tendency for a duct mode to follow a curved solid surface as it propagates. Refraction is the bending of the direction of duct mode propagation by a mean flow velocity gradient. It is shown that the mean flow velocity distribution around an engine inlet in forward flight differs markedly from that of an engine inlet in static operating condition. For this reason, there is a substantial change in the duct mode radiation pattern and directivity when switching from static condition to forward flight condition; however, as flight Mach number increases beyond 0.15, there are only minor changes in the mean flow. In other words, the forward flight effect exhibits a saturation phenomenon. This means that a further increase in forward flight Mach number above 0.15 would bring about little change in the duct mode radiation directivity.

In this investigation, a parametric study of the effect of frequency and azimuthal mode number on inlet acoustic radiation has been carried out. Both frequency and azimuthal mode number affect the axial wavelength of a duct mode. It is found that a change in axial wavelength affects the level of influence of both diffraction and refraction. Refraction exerts a larger impact on short waves than on long waves. Thus duct modes with higher frequencies or lower azimuthal mode numbers are more affected by refraction. On the other hand, diffraction has a larger effect on duct modes with long axial wavelengths. Because of these differences in axial-wavelength dependence, when the frequency or azimuthal mode number changes, the combined effect of diffraction and refraction will cause most duct modes at static condition to radiate at a relatively consistent angle in the sideline direction (approximately  $80^\circ$  inlet angle) but duct modes at forward flight condition to radiate at a range of angles in the forward direction.

A duct mode with a radial mode number  $n$  has  $n$  rows of alternating high- and low-pressure regions. Among these  $n$  rows, those that are closer to the casing surface at the casing lip region will be subjected to higher degrees of diffraction and refraction. This results in the splitting of the radiation pattern into multiple beams. The results of a brief study of this effect on duct modes with high-order radial mode numbers is reported.

It seems worthwhile to emphasize, based on the numerical simulation results of the present investigation, that the duct mode radiation pattern from a jet engine inlet in forward flight is quite different from that of an engine in static condition. For community noise prediction purposes, this suggests that there is no simple scaling formula that can convert the radiation pattern from the static condition to the flight condition. It is also recognized that there is no simple way to create a stagnation point, a distinct characteristic of forward flight, on the casing lip of an engine in a static test condition. Therefore, static engine test data might not be of use for engines in flight. Hence, the usefulness of such data may be very limited.

Before the advent of fast computers, sound radiation from engine inlets was investigated using a somewhat idealized model. The work of Wright (1972), Candel (1973) and Homicz & Lordi (1975) and others adopted a zero-thickness cylindrical inlet model. One main advantage of such a model is that the duct mode radiation problem can be solved exactly by the Wiener–Hopf technique. These early works were later summarized and extended by Rice, Heidmann & Sofrin (1979) to form a prediction formula for the direction of peak noise radiation. The most general formula of Rice *et al.* (1979) was designed to be applicable to inlet radiation at static as well as at flight condition. In their paper, they pointed out that, in deriving their formula, only the mean flow convection effect was included. The refraction effect was entirely neglected. In a real engine, the engine casing has a finite thickness. As was discussed in § 5, this thickness is very important to the processes of diffraction and refraction. Setting this thickness to zero may lead to severe prediction error.

As an illustration of the influence of inlet casing thickness on the effect of diffraction, a comparison between the computed peak direction of radiation from an SDT engine inlet using numerical simulation and that from a zero-thickness cylindrical inlet of the same diameter using the Rice *et al.* (1979) theory (in the absence mean flow) is made. Figure 50 shows a comparison of the computed peak directions of radiation for a duct mode with  $m = 22$  and  $n = 1$  as a function of frequency. The relevant parameter, important to the diffraction process, is the ratio of casing thickness to the axial wavelength of the duct mode. For the SDT inlet, this ratio is finite; for the zero-thickness cylindrical inlet, this ratio is zero. At low frequencies, the duct mode



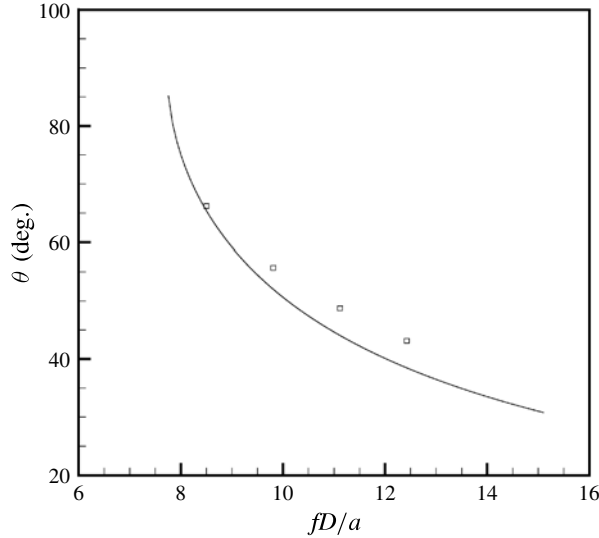


FIGURE 50. Peak direction of radiation for a duct mode with  $m = 22$ ,  $n = 1$  as a function of dimensionless frequency with no mean flow: —, Rice *et al.* (1979) theory (zero-thickness cylindrical inlet);  $\square$ , numerical simulation (SDT engine inlet).

axial wavelength is long, so the thickness-to-wavelength ratio is small. In this case, one would expect the two predictions to be fairly close. This is confirmed in figure 50. As frequency increases, this ratio becomes larger and larger for the SDT inlet. It follows that the difference between the two computed peak directions of radiation becomes larger and larger. This is also evident in figure 50.

As an illustration of the importance of including mean flow refraction in the prediction of duct mode radiation, a comparison is made between the result of using the classical theory of Rice *et al.* (1979) and that obtained by numerical simulation for the SDT engine inlet at static test condition. Figure 51 shows the peak directions of radiation for a duct mode with  $m = 22$  and  $n = 1$  at different dimensionless frequencies. It is clear that there are huge differences between the two predictions. Based on this result and the comparisons made in figure 50, we conclude that, for an accurate prediction of jet engine inlet acoustic radiation, it is imperative that the physical processes of diffraction and refraction be properly incorporated in the formulation of a theory or a computational model.

#### Appendix. Extension of near acoustic field to far field by the surface Green's function method

For the jet engine inlet noise radiation problem, a good matching surface for the extension of near field to far field is an infinitely long cylindrical surface enclosing the engine. For convenience, we set the matching cylindrical surface to be three mesh points inside the computational domain of figure 3. The generator of the cylindrical surface is parallel to the line BD. In all the validation directivity computations, the computational domain is extended to a distance of 10 fan diameters in the axial direction from the fan face and three fan diameters to the right of the line DF in figure 3. This extended domain is eight diameters larger than the computational domain for the near-field pressure contour study. This larger computational domain

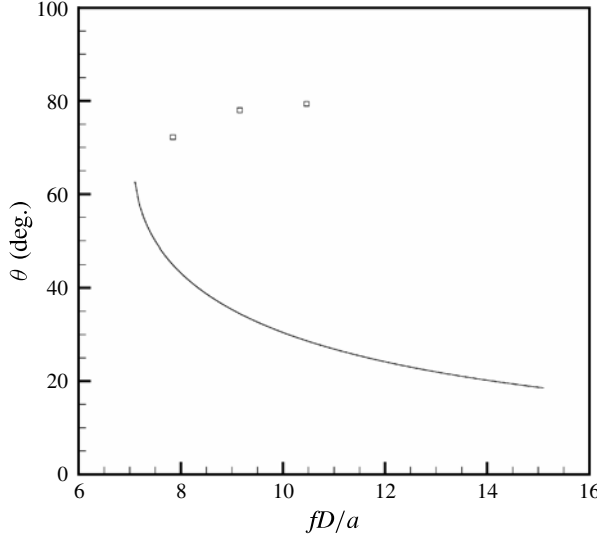


FIGURE 51. Peak direction of radiation for a duct mode with  $m = 22$ ,  $n = 1$  as a function of dimensionless frequency; static engine test with  $M_{fan} = 0.4$ : —, Rice *et al.* (1979) theory (zero-thickness cylindrical inlet);  $\square$ , numerical simulation (SDT engine inlet).

ensures that most of the sound waves radiated from the engine inlet pass through the matching surface.

Let the diameter of the matching cylindrical surface be  $D_M$  and the forward flight Mach number be  $M_\infty$  (i.e.  $M_\infty = M_{flight}$ ). Outside the matching cylindrical surface, the linearized Euler equation and energy equations are

$$\frac{\partial \mathbf{v}}{\partial t} + M_\infty \frac{\partial \mathbf{v}}{\partial x} = -\nabla p, \quad (\text{A } 1)$$

$$\frac{\partial p}{\partial t} + M_\infty \frac{\partial p}{\partial x} + \nabla \cdot \mathbf{v} = 0. \quad (\text{A } 2)$$

Upon eliminating  $\mathbf{v}$  from (A 1) and (A 2), the governing equation for  $p$  is

$$\left( \frac{\partial}{\partial t} + M_\infty \frac{\partial}{\partial x} \right)^2 p - \nabla^2 p = 0. \quad (\text{A } 3)$$

The surface Green's function  $G(r, \varphi, x, t; \varphi_0, x_0, t_0)$ , where  $(r, \varphi, x, t)$  are the far-field observer coordinates and time and  $(\varphi_0, x_0, t_0)$  are the source coordinates on the matching surface and time, satisfies the same governing equation as  $p$  (equation (A 3)), together with boundary conditions as follows:

$$\left( \frac{\partial}{\partial t} + M_\infty \frac{\partial}{\partial x} \right)^2 G - \nabla^2 G = 0, \quad (\text{A } 4)$$

$$\text{at } (r^2 + x^2)^{1/2} \rightarrow \infty, \quad G \text{ behaves as outgoing waves,} \quad (\text{A } 5)$$

$$\text{at } r = \frac{1}{2}D_M, \quad G = \frac{\delta(x - x_0)\delta(\varphi - \varphi_0)\delta(t - t_0)}{\frac{1}{2}D_M}. \quad (\text{A } 6)$$

Let the radiated pressure field be from a duct mode of azimuthal mode number  $m$ , radial mode number  $n$  and frequency  $\Omega$ . On the matching surface, the pressure field is

$$p = \text{Re}\{\hat{p}(x)e^{i(m\varphi - \Omega t)}\}. \quad (\text{A } 7)$$

By means of the Green's function, the sound field at a far-field point  $(r, \varphi, x, t)$  is given by

$$p(r, \varphi, x, t) = \text{Re} \left\{ \int_{-\infty}^{\infty} \int_{-\infty}^{\infty} \int_0^{2\pi} \hat{p}(x_0) e^{i(m\varphi_0 - \Omega t_0)} G(r, \varphi, x, t; \varphi_0, x_0, t_0) \frac{D_M}{2} d\varphi_0 dx_0 dt_0 \right\}. \quad (\text{A } 8)$$

To find  $G$ , let its Fourier transform in  $x$  and  $t$  be  $\hat{G}$ , defined as

$$\hat{G}(r, \varphi, k, \omega; \varphi_0, x_0, t_0) = \frac{1}{(2\pi)^2} \int_{-\infty}^{\infty} \int_{-\infty}^{\infty} G(r, \varphi, x, t; \varphi_0, x_0, t_0) e^{-i(kx - \omega t)} dx dt. \quad (\text{A } 9)$$

We know that  $\hat{G}$  is periodic in  $\varphi$ . Thus,  $\hat{G}$  may be expanded as a Fourier series in  $\varphi$  in the form

$$\hat{G}(r, \varphi, k, \omega; \varphi_0, x_0, t_0) = \sum_{n=-\infty}^{\infty} g_n e^{in\varphi}. \quad (\text{A } 10)$$

On applying Fourier transforms in  $x$  and  $t$  to (A 4) and on expanding  $\hat{G}$  as in (A 10), it is easy to find that  $g_n$  is given by the solution of the Bessel equation,

$$\frac{d^2 g_n}{dr^2} + \frac{1}{r} \frac{dg_n}{dr} - \frac{n^2}{r^2} g_n + [(\omega - M_{\infty} k)^2 - k^2] g_n = 0. \quad (\text{A } 11)$$

From (A 6), the boundary condition for  $g_n$  at  $r = D_M/2$  is

$$g_n = \frac{1}{4\pi^3 D_M} e^{-i(kx_0 + n\varphi_0 - \omega t_0)}. \quad (\text{A } 12)$$

In deriving (A 12), the  $\delta$ -function expansion,

$$\delta(\varphi - \varphi_0) = \frac{1}{2\pi} \sum_{n=-\infty}^{\infty} e^{in(\varphi - \varphi_0)}, \quad (\text{A } 13)$$

has been used. The solution of (A 11) satisfying the radiation boundary condition at  $(r^2 + x^2)^{1/2} \rightarrow \infty$  and boundary condition (A 12) is

$$g_n = \frac{1}{4\pi^3 D_M} \frac{H_n^{(1)}[i(1 - M_{\infty}^2)^{1/2}(k - k_+)^{1/2}(k - k_-)^{1/2}r]}{H_n^{(1)}[i(1 - M_{\infty}^2)^{1/2}(k - k_+)^{1/2}(k - k_-)^{1/2}\frac{1}{2}D_M]} e^{-i(kx_0 + n\varphi_0 - \omega t_0)}, \quad (\text{A } 14)$$

where  $k_+ = \omega/(1 + M_{\infty})$ ,  $k_- = -\omega/(1 - M_{\infty})$  and  $H_n^{(1)}[\ ]$  is the  $n$ th-order Hankel function of the first kind. The branch cut of the square root function and the inverse  $k$  contour are as shown in figure 52.

On substituting solution (A 14) into (A 10) and performing inverse transforms, the surface Green's function is found to be

$$G = \sum_{n=-\infty}^{\infty} \frac{1}{4\pi^3 D_M} \int_{-\infty}^{\infty} \int_{-\infty}^{\infty} \frac{H_n^{(1)}[i(1 - M_{\infty}^2)^{1/2}(k - k_+)^{1/2}(k - k_-)^{1/2}r]}{H_n^{(1)}[i(1 - M_{\infty}^2)^{1/2}(k - k_+)^{1/2}(k - k_-)^{1/2}\frac{1}{2}D_M]} \times \exp\{i[k(x - x_0) - \omega(t - t_0) + n(\varphi - \varphi_0)]\} dk d\omega. \quad (\text{A } 15)$$

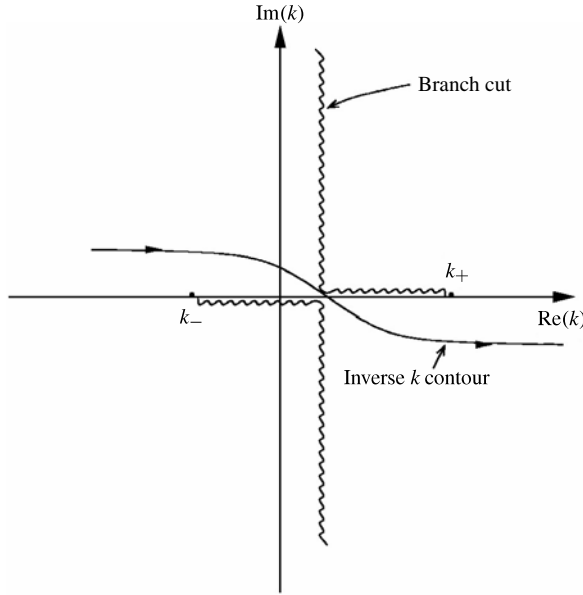


FIGURE 52. Branch cut for  $(k - k_+)^{1/2} (k - k_-)^{1/2}$  in the  $k$ -plane and the inverse Fourier transform contour.

For the far-field solution, it is advantageous to switch to spherical polar coordinates  $(R, \theta, \varphi)$  with the polar axis coinciding with the  $x$ -axis. The spherical polar coordinates and the cylindrical coordinates are related by

$$x = R \cos \theta, \quad r = R \sin \theta, \quad (\text{A } 16)$$

where  $\theta$  is the polar angle. Now, for  $R \rightarrow \infty$ ,  $G$ , as given by (A 15), may be greatly simplified by first using the asymptotic form of the Hankel function, then evaluating the  $k$  integral by the method of stationary phase. The stationary phase point is at  $k = (\omega/(1 - M_\infty^2))[\cos \theta / (1 - M_\infty^2 \sin^2 \theta)^{1/2} - M_\infty]$ . This gives

$$\begin{aligned}
 G = & \frac{1}{2\pi^3 D_M (1 - M_\infty^2 \sin^2 \theta)^{1/2} R} \sum_{n=-\infty}^{\infty} \int_{-\infty}^{\infty} \frac{\exp \left( \left\{ \frac{i\omega R}{M_\infty \cos \theta + (1 - M_\infty^2 \sin^2 \theta)^{1/2}} \right\} \right)}{H_n^{(1)} \left[ \frac{\omega D_M \sin \theta}{2 (1 - M_\infty^2 \sin^2 \theta)^{1/2}} \right]} \\
 & \times \exp \left( \frac{-i\omega}{(1 - M_\infty^2)} \left[ \frac{\cos \theta}{(1 - M_\infty^2 \sin^2 \theta)^{1/2}} - M_\infty \right] x_0 \right) \\
 & \times \exp \left( i \left[ n(\varphi - \varphi_0) - \omega(t - t_0) - (n + 1) \frac{\pi}{2} \right] \right) d\omega. \quad (\text{A } 17)
 \end{aligned}$$

On inserting the surface Green's function (A 17) into (A 8), the far-field pressure at  $R \rightarrow \infty$  corresponding to a duct mode of azimuthal mode number  $m$  and angular frequency  $\Omega$  can be found by evaluating the integrals  $d\varphi_0 dt_0 dx_0 d\omega$ . The  $d\varphi_0$  and  $dt_0$

integration can be carried out easily using

$$\int_0^{2\pi} e^{i(m-n)\varphi_0} d\varphi_0 = 2\pi\delta_{mn}, \quad (\text{A } 18)$$

$$\int_{-\infty}^{\infty} e^{-i(\Omega-\omega)t_0} dt_0 = 2\pi\delta(\omega - \Omega). \quad (\text{A } 19)$$

Because of the delta function  $\delta(\omega - \Omega)$  from (A 19), the  $d\omega$  integral can also be evaluated. This gives the following formula, which involves a single integral, for the far-field pressure,

$$p(R, \theta, \varphi, t) = \text{Re} \left\{ \frac{1}{\pi (1 - M_\infty^2 \sin^2 \theta)^{1/2} R} \times \left[ \frac{\exp \left( \frac{i\Omega R}{M_\infty \cos \theta + (1 - M_\infty^2 \sin^2 \theta)^{1/2}} + i \left[ m\varphi - \Omega t - (m+1) \frac{\pi}{2} \right] \right)}{H_m^{(1)} \left[ \frac{\Omega D_M \sin \theta}{2 (1 - M_\infty^2 \sin^2 \theta)^{1/2}} \right]} \right] \times I \right\}_{R \rightarrow \infty}, \quad (\text{A } 20)$$

where

$$I = \int_{-\infty}^{\infty} \hat{p}(x_0) \exp \left( \frac{-i\Omega}{(1 - M_\infty^2)} \left[ \frac{\cos \theta}{(1 - M_\infty^2 \sin^2 \theta)^{1/2}} - M_\infty \right] x_0 \right) dx_0. \quad (\text{A } 21)$$

## REFERENCES

- ACHUNCHE, I., ASTLEY, J., SUGIMOTO, R. & KEMPTON, A. 2009 Prediction of forward fan noise propagation and radiation from intakes. *AIAA Paper* 2009-3239.
- AHUJA, V., OZYORUK, Y. & LONG, L. N. 2000 Computational simulations of fore and aft radiation from ducted fans. *AIAA Paper* 2000-1943.
- ASTLEY, R. J., HAMILTON, J. A., BAKER, N. & KITCHEN, E. H. 2002 Modelling tone propagation from turbofan inlets – the effect of extended lip liners. *AIAA Paper* 2002-2449.
- BAUMEISTER, K. J. & HOROWITZ, S. J. 1984 Finite element-integral acoustic simulation of JT15D turbofan engine. *Trans. ASME: J. Vib. Acoust. Stress Reliab. Design* **106**, 405–413.
- CALLENDER, B., JANARDAN, B.,UELLENBERG, S., PREMIO, J., KWAN, H. W. & ABEYSINGHE, A. 2007 The Quiet Technology Demonstrator program: static test of an acoustically smooth inlet. *AIAA Paper* 2007-3671.
- CANDEL, S. M. 1973 Acoustic radiation from the end of a two-dimensional duct, effects of uniform flow and duct lining. *J. Sound Vib.* **28**, 1–13.
- CANTRELL, R. H. & HART, R. W. 1964 Interaction between sound and flow in acoustic cavities: mass, momentum and energy considerations. *J. Acoust. Soc. Am.* **36**, 697–706.
- DOUGHERTY, R. P. 1996 Nacelle acoustic design by ray tracing in three dimensions. *AIAA Paper* 96-1773.
- EVERSMAN, W., PARRETT, A. V., PREISSER, J. S. & SILCOX, R. J. 1985 Contributions to the finite element solution of the fan noise radiation problem. *Trans. ASME* **107**, 216–223.
- FFOWCS WILLIAMS, J. E. & HAWKINGS, D. L. 1969 Sound generation by turbulence and surfaces in arbitrary motion. *Proc. R. Soc. Lond. A* **264**, 321–342.

- HEIDELBERG, L. 2002 Fan noise source diagnostic test – tone modal structure results. *AIAA Paper* 2002-2428.
- HEIDELBERG, L. J., RICE, E. J. & HOMYAK, J. 1981 Acoustic performance of inlet suppressors on an engine generating a single mode. *AIAA Paper* 81-1965.
- HEIDMANN, M. F., SAULE, A. V. & MCARDLE, J. G. 1980 Predicted and observed modal radiation pattern from JT15D engine with inlet rods. *J. Aircraft* **17**, 493–499.
- HERKES, W. H., OLSEER, R. F. & UELLENBERG, S. 2006 The Quiet Technology Demonstrator program: flight validation of airplane noise-reduction concepts. *AIAA Paper* 2006-2720.
- HOMICZ, G. F. & LORDI, J. A. 1975 A note on the radiative directivity patterns of duct acoustic modes. *J. Sound Vib.* **41**, 283–290.
- HU, F. Q. 2001 A stable perfectly matched layer for linearized Euler equations in unsplit physical variables. *J. Comput. Phys.* **173**, 455–480.
- HU, F. Q. 2008 Development of PML absorbing boundary conditions for computational aeroacoustics: a progress review. *Comput. Fluids* **37**, 336–348.
- KEMPTON, A. J. & SMITH, M. G. 1982 Ray theory predictions of sound radiation from realistic engine intakes. *AIAA Paper* 81-1982.
- LAN, J., PREMO, J., ZLAVOG, G., BREAD, C., CALLENDER, B. & MARTINEZ, M. 2007 Phased array measurements of full-scale engine inlet noise. *AIAA Paper* 2007-3434.
- LANSING, D. L. 1970 Exact solution for radiation of sound from a semi-infinite circular duct with application to fan and compressor noise. *Analytic Methods in Aircraft Aerodynamics*, NASA SP-228, pp. 323–334.
- LYRINTZIS, A. S. 2003 Surface integral methods in computational aeroacoustics – from the (CFD) near-field to the (acoustic) far-field. *Intl J. Aeroacoust.* **2**, 95–128.
- OZYORUK, Y. 2002 Parallel computation of forward radiated noise of ducted fans including acoustic treatment. *AIAA J.* **40**, 450–455.
- OZYORUK, Y., AHUJA, V. & LONG, L. N. 2001 Time domain simulations of radiation from ducted fans with liners. *AIAA Paper* 2001-2171.
- OZYORUK, Y., ALPMAN, E., AHUJA, V. & LONG, L. N. 2004 Frequency-domain prediction of turbofan noise radiation. *J. Sound Vib.* **270**, 933–950.
- OZYORUK, Y. & LONG, L. N. 1996 Computation of sound radiation from engine inlets. *AIAA J.* **34**, 894–901.
- PARRETT, A. & EVERSMA, W. 1986 Wave envelope and finite element approximation for turbofan noise radiation in flight. *AIAA J.* **24**, 753–760.
- PILON, A. R. & LYRINTZIS, A. S. 1998 Development of an improved Kirchhoff method for jet aeroacoustics. *AIAA J.* **36**, 783–790.
- PREISSER, J. S., SILCOX, R. J., EVERSMA, W. & PARRETT, A. V. 1985 Flight study of induced turbofan acoustic radiation with theoretical comparisons. *J. Aircraft* **22**, 57–62.
- PREMO, J., BREAD, C. & LAN, J. 2007 Prediction of the inlet splice effects from the QDT2 static test. *AIAA Paper* 2007-3544.
- PREMO, J. & JOPPA, P. 2002 Fan noise source diagnostic test – wall measured circumferential array mode results. *AIAA Paper* 2002-2429.
- REBA, R. A., NARAYANA, S., COLONIUS, T. & SUZUKI, T. 2005 Modelling jet noise from organized structures using near-field hydrodynamics pressure. *AIAA Paper* 2005-3093.
- REBA, R. A., SIMONICH, J. & SCHLINKER, R. 2008 Measurement of source wave-packets in high-speed jets and connection to far-field sound. *AIAA Paper* 2008-2891.
- RICE, E. J., HEIDMANN, M. F. & SOFRIN, T. G. 1979 Modal propagation angles in a cylindrical duct with flow and their relation to sound radiation. *AIAA Paper* 79-0183.
- ROY, I. D. & EVERSMA, W. 1995 Improved finite element modelling of the turbofan engine inlet radiation problem. *Trans. ASME: J. Vib. Acoust.* **117**, 109–115.
- SHEN, H. & TAM, C. K. W. 2002 Three-dimensional numerical simulation of the jet screech phenomenon. *AIAA J.* **36**, 33–41.
- TAM, C. K. W. 1998 Advances in numerical boundary conditions for computational aeroacoustics. *J. Comput. Acoust.* **6**, 377–402.
- TAM, C. K. W. 2012 *Computational Aeroacoustics: a Wavenumber Approach*. Cambridge University Press.

- TAM, C. K. W. & DONG, Z. 1996 Radiation and outflow boundary conditions for direct computation of acoustic and flow disturbances in a non-uniform mean flow. *J. Comput. Acoust.* **4**, 175–201.
- TAM, C. K. W. & HU, F. Q. 2004 An optimized multi-dimensional interpolation scheme for computational aeroacoustics applications using overset grid. *AIAA Paper* 2004-2812.
- TAM, C. K. W. & JU, H. 2012 Airfoil tones at moderate Reynolds number. *J. Fluid Mech.* **690**, 536–570.
- TAM, C. K. W. & KURBATSKII, K. A. 2003 Multi-size-mesh multi-time step dispersion relation preserving scheme for multiple-scales aeroacoustics problems. *Intl J. Comput. Fluid Dyn.* **17**, 119–132.
- TAM, C. K. W., PASTOUCHENKO, N. N. & VISWANATHAN, K. 2010 Continuation of the near acoustic field of a jet to the far field. Part I. Theory. *AIAA Paper* 2010-3728.
- TAM, C. K. W. & WEBB, J. C. 1993 Dispersion-relation-preserving scheme for computational acoustics. *J. Comput. Phys.* **107**, 262–281.
- WHITE, F. M. 1991 *Viscous Fluid Flow*, 2nd edn. McGraw-Hill.
- WOODWARD, R. P., HUGHES, C. E., JERACKI, R. J. & MILLER, C. J. 2002 Source diagnostic test – far field acoustic results. *AIAA Paper* 2002-2427.
- WRIGHT, S. E. 1972 Waveguides and rotating sources. *J. Sound Vib.* **25**, 163–178.
- YU, J., NESBITT, E., KWAN, H. W.,UELLENBERG, S., CHIEN, E., PREMO, J., RUIZ, M. & CZECH, M. 2006 Quiet Technology Demonstrator 2 intake liner design and validation. *AIAA Paper* 2006-2458.
- ZHANG, X., CHEN, X., MORFEY, C. L. & NELSON, P. A. 2002 Computation of spinning modal radiation from an unflanged duct. *AIAA Paper* 2002-2475.